Azimuthal Anisotropy From Multimode Waveform Modeling Reveals Layering Within the Antarctica Craton

Caroline Beghein * [1], **Haotian Xu** [1]

[1]Department of Earth, Planetary, and Space Sciences, University of California Los Angeles, Los Angeles, CA, USA

Author contributions: *Conceptualization*: C. Beghein. *Methodology*: C. Beghein, H. Xu. *Software*: H. Xu. *Formal Analysis*: C. Beghein, H. Xu. *Writing - original draft*: C. Beghein. *Visualization*: H. Xu. *Supervision*: C. Beghein.

Abstract The isotropic structure of the crust and upper mantle under Antarctica has been constrained by many studies. However, the depth dependence of seismic anisotropy, a powerful tool to characterize deformation and flow, is still poorly known. Here, we modeled three-dimensional (3-D) variations in azimuthal anisotropy under Antarctica using a multimode Rayleigh waveform fitting technique. We first searched the model space with a reversible-jump Markov Chain Monte Carlo approach to find path-averaged vertically polarized shear wave velocity profiles that fit fundamental and higher mode Rayleigh waveforms. We then inverted them to obtain a 3-D velocity and azimuthal anisotropy model across the region down to 600 km depth. Our results reveal that the east-west dichotomy found in other studies is not only characterized by different wave velocities but also by different anisotropy directions, likely reflecting the different deformation histories of the two blocks. Azimuthal anisotropy was found to be present in the top 300 km only and peaks at 100 — 200 km depth under the East Antarctica craton. Additionally, depth changes in fast direction were observed within the craton between 75 km and 150 km depth, suggesting layering is present. We speculate this layering relates to the formation history of the craton.

Non-technical summary The Antarctica plate holds important clues regarding continent formation and evolution. The dependence of the speed of seismic waves with the wave direction of propagation provides unique information about the deformation history of the crust and mantle. However, few studies so far have constrained the depth extent of the anisotropy below 200 km depth. Here we use recordings of distant earthquakes over a 15 year period at seismometers across and around Antarctica to investigate the presence of anisotropy down to 600 km depth. We find that anisotropy is present across the continent in the upper 300 km but not deeper. There is also a striking difference in the fast wave direction between the oldest part of Antarctica to the East and the younger West Antarctica. Our results also indicate a vertical change in anisotropy between

*Corresponding author: cbeghein@ucla.edu

75 km and 150 km depth under the oldest, most stable part of the continent. We speculate it relates to compositional changes linked to the building of the history of formation of the continent.

1 Introduction

1.1 Tectonic Setting

The Antarctica plate, which includes the Antarctica continent, the Kerguelen Plateau, and oceans, is one of the largest plates on Earth. It is interesting from a tectonics and geodynamics point of view as its structure holds important clues regarding the reconstruction of the supercontinent Gondwana (e.g. Boger, 2011; Ebbing et al., 2021). It also moves relatively slowly compared to other large plates (at 1.89 cm/yr in West Antarctica in a no-net rotation reference (NNR) frame (Accardo et al., 2014)). The continent can be divided into two distinct regions (Fig. 1): East Antarctica (EANT), which is believed to be a Precambrian craton, and West Antarctica (WANT), which is composed of several crustal blocks dating back to the Jurassic (Dalziel, 1992; Anderson, 1999). Between EANT and WANT, the 3,500 km-long Transantarctic Mountains (TAMs) extend from Victoria Land in the South to the Weddell Sea in the North (Fitzgerald, 2002). A notable feature at the center of EANT is the high elevation (>2,000 m) Gamburtsev Subglacial Mountain (GSM) chain, but its age and origin are not well constrained because they are hidden beneath the East Antarctic Ice Sheet (Ferraccioli et al., 2011). WANT includes the West Antarctic Rift System (WARS), a striking geological feature that experienced extension starting after the break-up of Australia and Antarctica 95 Ma ago, and that has been active during most of the Cenozoic (e.g. Behrendt, 1999; Wörner, 1999; Granot et al., 2010). A thermal anomaly related to this extension is thought to be present in the WANT asthenosphere (An et al., 2015a). WANT is also comprised of the Marie Byrd Land (MBL), which is associated with recent volcanism that might have resulted from the rifting or that may instead reflect the signature of a mantle plume (Behrendt et al., 1991) as suggested by seismology (e.g. Sieminski et al., 2003; Accardo et al., 2014; Emry et al., 2015) and geochemistry (Wörner, 1999).

1.2 Seismic Velocities

Early seismological studies of Antarctica generally suffered from poor resolution due to the paucity of seismic stations (e.g. Press and Gilbert, 1959; Evison et al., 1960; Kovach and Press, 1961; Dewart and Toksöz, 1965; Roult et al., 1994; Sieminski et al., 2003). However, seismic deployments over the past two decades have greatly improved data coverage and have led to several higher resolution models of the Antarctic crust and upper mantle (e.g. Heeszel et al., 2013; Hansen et al., 2014; An et al., 2015b; Lloyd et al., 2015).

Seismological studies generally agree that EANT is characterized by a thick crust and a deep root with relatively fast seismic velocities that are typically representative of stable continents, whereas WANT displays lower velocities and a thinner crust (Roult et al., 1994; Danesi and Morelli, 2000, 2001; Ritzwoller et al., 2001; Sieminski et al., 2003; Watson et al., 2006; Hansen et al., 2010; Heeszel et al., 2013; An et al., 2015b; Lloyd et al., 2020) and no clear signature of a fast lid (Ritzwoller et al., 2001). The first estimates of Moho depths (Evison et al., 1960; Kovach and Press, 1961; Dewart and Toksöz, 1965) were around $35-40$ km and $25-30$ km for EANT and WANT, respectively. More recent analyses show an average Moho of $\sim$40 km in the central EANT region, $19-29$ km for WARS (Ramirez et al., 2016), and 43 — 58 km underneath the GSM (Hansen et al., 2009, 2010; Ramirez et al., 2016). The latter is generally larger than the 40 km from gravity analyses at the GSM (Block et al., 2009). For the Ross Sea, the WANT crustal thickness ranges between 16 and 25 km (Winberry and Anandakrishnan, 2004; Lawrence et al., 2006; Pyle et al., 2010; Finotello et al., 2011; Chaput et al., 2014; Ramirez et al., 2017). At MBL, values of 20 — 35 km have been reported (Ramirez et al., 2016, 2017). Ramirez et al. (2016) additionally estimated heat flow from their Moho depth measurements and the age of the crust. They found values under the GSM and the Wilkes Subglacial Basin (WILK) similar to Precambrian terrains on other continents where heat flow has been measured.

Most studies point to a maximum lithospheric thickness of around 250 km under EANT, though most do not have great vertical resolution below that depth. In the first tomographic model of Antarctica, Roult et al. (1994) detected a structure characterized by fast seismic velocities down to depths of about 250 km under EANT. Ritzwoller et al. (2001) found similar values with a continental root of 220-250 km and no low-velocity zone, and Danesi and Morelli (2001) reported values of at least 200 km. New surface wave analyses of fundamental mode phase (Heeszel et al., 2013) and group (An et al., 2015b) velocities show similar and consistent results for EANT: the Gamburtsev Subglacial Mountains (GSM) are underlaid by a thick crust ($\sim$60 km) and a seismically fast cratonic lithosphere reaching deeper than 200 km. The exception is the full-waveform adjoint tomography of Lloyd et al. (2020) that led to a greater cratonic thickness between 250 km and 350 km.

The TAMs as well as the ocean ridges surrounding the Antarctic continent are generally characterized by low velocities mostly confined to the upper 150 km (Roult et al., 1994; Danesi and Morelli, 2001; Watson et al., 2006). The volcanism at the Victoria Land segment of the TAMs (e.g. Mount Erebus) is commonly thought to have a deep mantle origin (Emry et al., 2020) and is often attributed to mantle plumes (LeMasurier and Landis, 1996). A localized low-velocity region down to about 200 km depth under the Ross Island volcanic complex was also detected (Danesi and Morelli, 2001; Watson et al., 2006), superimposed to the broader anomaly associated with the WARS (Morelli and Danesi, 2004; Danesi and Morelli, 2001). Based on the inversion of fundamental and higher mode Rayleigh waves dispersion, Sieminski et al. (2003) argued that this relatively slow structure extends into the mantle transition zone (MTZ) and indicates the presence of a mantle plume. A number of recent regional seismic tomographic results have also shown relatively low seismic velocities under the MBL extending through the upper mantle and possibly into the mantle transition zone (Hansen et al., 2014; Lloyd et al., 2015; Heeszel et al., 2016; Lloyd et al., 2020). In contrast, Emry et al. (2015) detected a local thinning of the transition zone, which may indicate high mantle temperatures, beneath neighboring areas of MBL rather than right below MBL.

1.3 Seismic Anisotropy

Seismic anisotropy, i.e., the directional dependence of seismic wave velocity, offers a more complete description of Earth's elastic structure than isotropic velocities alone. It is also a powerful tool to constrain patterns of deformation in the mantle or the crust (e.g. Becker et al., 2003; Karato et al., 2008; Volk et al., 2021). Anisotropy can manifest itself in different ways in seismic observations: (1) Azimuthal anisotropy, which describes the dependence of seismic wave speeds on the propagation azimuth; and (2) transverse isotropy, in which case the elastic medium has one axis of symmetry. The wave speed differs along the symmetry axis and in the orthogonal direction. This type of anisotropy is referred to as radial anisotropy if the symmetry axis points toward the center of the planet (radial direction).

Two different mechanisms can yield observations of seismic anisotropy: The shape-preferred orientation (SPO) of isotropic structures with contrasting elastic properties and the lattice-preferred orientation (LPO) of the crystallographic axes of elastically anisotropic minerals. LPO of olivine is the generally accepted explanation for observations of seismic anisotropy in the upper mantle as its crystals are highly anisotropic (about 18% shear-wave anisotropy) and is thought to be the dominant material at those depths (Karato and Wu, 1993). In addition, most olivine deformation fabrics tend to align the fast axes of individual olivine crystals in the direction of shear. In the case of horizontal mantle flow induced by a vertical velocity gradient, the rule of thumb is thus that the fast direction for seismic waves reflects the flow direction. Consequently, observations of seismic anisotropy with axes aligned with present-day plate motion in regions of low seismic velocities are often interpreted as the signature of current mantle flow in the asthenosphere (e.g. Gung et al., 2003; Marone et al., 2007; Beghein et al., 2014). In the mantle lithosphere, it has been interpreted as the signature of fossil- or paleo-directions of deformation (e.g. Silver, 1996; Smith et al., 2004). Seismic anisotropy has also been detected at greater depths, including in the mantle transition zone (e.g. Fouch and Fischer, 1996; Trampert and van Heijst, 2002; Visser, 2008; Yuan and Beghein, 2013; Auer et al., 2014; Yuan and Beghein, 2014; Huang et al., 2019), top of the lower mantle (e.g. Lynner and Long, 2015; Ferreira et al., 2019), and in the lowermost mantle (e.g. Panning and Romanowicz, 2006; Lynner et al., 2014), but its interpretation at those depths is more uncertain.

Shear-wave splitting (e.g. Silver and Chan, 1988; Long and van der Hilst, 2005) is one of the most common types of seismic observations that can directly detect the presence of seismic anisotropy, and a number of researchers have applied this technique to Antarctica (e.g. Pondrelli and Azzara, 1998; Barruol and Hoffmann, 1999; Müller, 2001; Pondrelli et al., 2006; Bayer et al., 2007; Reading and Heintz, 2008; Barklage et al., 2009). With the seismometers deployed for the POLENET/ANET project, Accardo et al. (2014) carried out analyses of azimuthal anisotropy for WANT. They found that the fast axis directions for shear waves consistently show large angles with the Absolute Plate Motion (APM), which may indicate that the uppermost mantle is subject to a secondary convection mechanism other than plate motion. They also found a radial pattern of fast axis direction inland from the Amundsen Sea around the MBL dome, which was interpreted as flow associated with a mantle plume head.

Another body wave technique, based on P-wave travel times, was also applied to data collected by multiple arrays in northeast Antarctica, covering the northern TAMs, the WILK, and the Terror Rift, which is located at the westernmost edge of the WARS (Zhang et al., 2020). The authors detected lateral variations in P-wave radial anisotropy at depths < 300 km with a fast horizontal direction associated with past tectonic events under the northern TAMs. They also found that the Terror Rift is associated with a fast vertical direction, which they attributed to local asthenospheric upwelling. The same study revealed a high-velocity zone under the TAMs and below 300 km depth, which, combined with the radial anisotropy, was interpreted as being due to a foundering lithosphere or a delaminated slab.

Body wave analyses provide good lateral resolution, but they lack vertical resolution because measurements result from near-vertical paths and thus reflect the integrated effect of the (anisotropic) structures encountered along the path. Surface waves constitute another type of data that can be used to model seismic anisotropy (e.g. Anderson, 1962; Montagner and Nataf, 1986; Ekström and Dziewonski, 1998; Trampert and van Heijst, 2002; Trampert and Woodhouse, 2003). Even though their lateral resolution (of a few hundred of kilometers at best) is lower than that of body waves, they provide constraints on structure and anisotropy with greater vertical resolution due to their dispersive nature. Roult et al. (1994) obtained the first azimuthally anisotropic phase velocity maps of Antarctica by inverting fundamental mode Rayleigh wave dispersion curves in the period range 60 — 300 s. Their study, which covered the whole Antarctica continent and its surroundings, showed that oceanic areas are associated with stronger azimuthal anisotropy than continents and that the TAMs have relatively large anisotropy within the Antarctica continent. The fast directions of propagation in the oceans were found to be orthogonal to most of the ridges and to align with the direction of plate motion. However, the ray path coverage was very limited due to the small number of stations available, with only ∼400 paths covering the southern hemisphere. Ritzwoller et al. (2001) performed another continental-scale study of the region and reported an average of ∼4 % radial anisotropy for Antarctica and surrounding areas, with slightly stronger amplitudes in WANT than in EANT.

Additionally, with data from the Transantarctic Mountain Seismic Experiment, Lawrence et al. (2006) measured Rayleigh wave dispersion under the Ross Sea, the TAMs, and EANT with an interstation technique, and detected 1.5 — 3% azimuthal anisotropy beneath EANT with a NE-SW fast direction at periods between 20 and 120 s, corresponding to depths of ∼30 — 160 km. They attributed this anisotropy to LPO within a cold continental lithosphere due to past deformation such as the Ross Orogeny. It should be noted that because their anisotropy model was found to be reliable only at the intersection of the two seismic arrays they used, they did not have constraints on the lateral extent of the anisotropy.

More recently, seismic anisotropy was also discovered in the crust and uppermost mantle across WANT and central Antarctica using ambient noise tomography in the period range 8 — 25 s (O'Donnell et al., 2019; Zhou et al., 2022, 2023). Radial anisotropy with horizontally polarized shear (SH) waves faster than vertically polarized shear (SV) waves and azimuthal anisotropy were found in the shallow crust. The fast direction of the azimuthal anisotropy is subparallel to the inferred extension direction of the West Antarctic Rift System (Zhou et al., 2023). This is consistent with LPO of minerals such as mica and amphibole in extensional settings. Most of West and Central Antarctica display a mid-to-lower crust with $V_{SV} > V_{SH}$ instead, potentially due to LPO of plagioclase under extension. The uppermost mantle under WANT was shown to be characterized by $V_{SH} > V_{SV}$, interpreted as olivine LPO due to tectonic activity (Zhou et al., 2022). This is supported by the azimuthal anisotropy fast direction that generally aligns with shear wave splitting fast axes and suggests a thin lithosphere (Zhou et al., 2023).

Because body wave studies have limited vertical resolution and the surface wave results discussed above were based on data that cannot resolve structure below ~ 200 km, the depth extent of seismic anisotropy under Antarctica is still poorly known. Higher mode surface waves have the potential to improve our constraints on the depth dependence of anisotropy as they are sensitive to much larger depths than fundamental mode surface waves or ambient noise data. To the best of our knowledge, only two studies of Antarctica have utilized such surface wave overtones: (1) Sieminski et al. (2003), who found the presence of azimuthal anisotropy to be significant in the upper 200 km underneath the Antarctica continent, with maximum amplitudes at 100 km depth, and decreasing to less than 1 % below 200 km, and (2) Lloyd et al. (2020), but they did not interpret the radial anisotropy structure retrieved due to an imbalance in sensitivity of the speed of SV and SH waves.

In this paper, we took advantage of the increased number of available seismic stations in Antarctica since the study of Sieminski et al. (2003), and we obtained a new three-dimensional azimuthally anisotropic model for SV waves down to 600 km depth by jointly inverting fundamental and higher mode Rayleigh waveforms. We first present the data and methods employed, present our model, and interpret it in terms of deformation mechanisms. We then put it in the context of previous surface wave and shear wave splitting studies.

2 Data Selection

The seismic data coverage in Antarctica was boosted significantly by the deployment of temporary seismic networks (e.g., TAMSEIS (Anandakrishnan and Wiens, 2000), GAMSEIS (Wiens and Nyblade, 2007a), POLENET (Wiens and Nyblade, 2007b), TAMNNET (Hansen, 2012), UKANET (Alex Brisbourne et al., 2016)). In this study, we considered permanent and temporary seismic stations south of -40 degrees latitude and collected data recorded between 2005 and 2020. Because the lateral resolution of the models is limited by the wavelength of the surface wave data utilized, performing measurements at nearby stations would not improve resolution. The minimum interstation distance was thus set at 75 km so that only a few stations from dense arrays are used. The list of stations employed can be found in Tab. S1. The selected 168 stations are shown in Fig. 2.

We considered all events recorded at these stations between 2005 and 2020 and falling between -20 degrees to -90 degrees latitude. We obtained the event source parameters from the GCMT catalog (Dziewonski et al., 1981; Ekström et al., 2012), and selected events with moment magnitudes Mw between 5.5 and 7.0. The magnitude thresholds were chosen to avoid small magnitude earthquakes with a low signal-to-noise ratio (SNR), and to avoid large magnitude earthquakes that cannot be approximated by the single point source assumption in waveform modeling. The station-event pairs were then selected based on the following criteria: 1) The epicentral distance should be between 30 degrees and 75 degrees. The lower bound guarantees that the higher mode waveforms separate adequately from the fundamental mode. We also avoided paths with long epicentral distances as they are more likely to be contaminated by scattering effects (Lebedev et al., 2005); 2) The SNR of the recorded waveform should be higher than 10 for the 10-20 mHz frequency band, and higher than 5 for the 5-10 mHz frequency band. This second criterion helped filter out records contaminated by noise. The lower frequency band had a lower threshold because it usually carries weaker energy compared to the higher frequency band; 3) At least 45 % of the great circle paths had to fall within the Arctic Circle in order to ensure good constraints on the Antarctica Continent. The selected 578 events are shown in Fig. 2 and the corresponding ray coverage is in Fig. 3.

3 Methods

Higher mode surface waves have the advantage of being sensitive to a greater depth range than the traditionally used fundamental mode surface waves at the same periods. They are also dispersive and this dispersion relation can be employed to constrain the depth dependence of seismic wave velocities and anisotropy. Measuring higher modes surface wave dispersion is, however, challenging because their group velocities overlap significantly in a broad frequency range. Therefore, direct measurement methods that work for fundamental mode surface waves cannot be applied to higher modes due to the difficulties in separating different modes. Waveform fitting techniques have been favored by multiple researchers instead (Stutzmann and Montagner, 1993; Montagner et al., 1994; Beucler et al., 2003;

Yoshizawa and Kennett, 2002, 2004; Yoshizawa and Ekström, 2010; Visser et al., 2007; Visser, 2008; Xu and Beghein, 2019). In this study, we opted to use the waveform-fitting method developed by Xu and Beghein (2019). It was initially designed to separate different modes and measure single-station phase velocity dispersion curves for fundamental mode surface waves and overtones, which in turn can be inverted for structure. Our waveform modeling approach can also be used directly to obtain a 3-D interior model, which is what we opted to do in this study, as explained below.

3.1 Waveform Fitting

The method employed makes use of a reversible-jump Markov Chain Monte Carlo (rj-MCMC) approach (Bodin and Sambridge, 2009; Bodin et al., 2012) and performs a transdimensional model space search to seek a large number of path-averaged one-dimensional (1-D) shear wave velocity (V_S) models that fit the filtered waveform. Here, we filtered the waveforms between 50 s and 200 s period. In the original version of the software, the resulting 1-D models, which represent the average fundamental and higher-mode dispersion curves for the chosen source-receiver path, were employed to calculate dispersion curves. A reliability analysis was performed afterwards to determine which overtones had been reliably separated. Here, we invert the 1-D path-averaged models instead to construct a 3-D model of shear-wave velocities and anisotropy and skip the phase velocity dispersion estimate (see details in section 3.2).

A synthetic seismogram, denoted by s, can be calculated by summation of normal modes, m, in the frequency domain for a 1-D model as follows (Dahlen, 1968):

$$s(\omega) = \sum_m A_m(\omega) exp[i\omega\Delta/c_m(\omega)] \quad (1)$$

where $c_m(\omega)$ is the phase velocity of mode m at angular frequency ω, A_m is its amplitude, and Δ is the epicentral distance. The relationship between seismograms and their corresponding velocity model is thus highly non-linear. The computation of normal mode eigenfunctions and eigenfrequencies for a given mantle model is time-consuming and thus we cannot use the fully non-linear formulation of Eq. 1 at each of the hundreds of thousands of iterations of the MCMC scheme. The forward modeling problem was thus linearized to overcome computational speed limitations as detailed in the next paragraph.

A synthetic seismogram is first obtained for a chosen reference model using the fully non-linear formulation of Eq. 1 and FORTRAN package Mineos (Masters et al., 2011). Perturbation theory is then applied to update the seismogram for the models generated at each iteration of the Markov Chain. For a small perturbation, the change in mode eigenfrequency can be calculated assuming unperturbed eigenfunctions:

$$\delta\ln(\omega) = \int_0^a \left(\frac{\delta V_P}{V_P}(r)K_{V_P}(r,\omega) + \frac{\delta V_S}{V_S}(r)K_{V_S}(r,\omega) + \frac{\delta\rho}{\rho}(r)K'_\rho(r,\omega)\right)dr + \sum_d \delta d[K_d(\omega)]^+_- \quad (2)$$

where $\delta\ln(\omega) = \delta\omega/\omega$, a is the radius of the Earth, and V_P, V_S, ρ and d are P-wave velocity, S-wave velocity, density, and radius of discontinuities, respectively. $K_{V_P}, K_{V_S}, K'_\rho$ and K_d are the Fréchet derivatives, which relate the change in wave velocities, density, and depth of discontinuity from the reference model to changes in the eigenfrequencies. The Fréchet derivatives are calculated for each mode using the eigenfunctions determined for the reference model (Woodhouse, 1980). The updated eigenfrequency ω^* can be converted into phase velocity for a normal mode of angular order l using (Jeans, 1923):

$$c(\omega^*) = \frac{\omega^* a}{l + 0.5} \tag{3}$$

The isotropic nature of the model is assumed at this stage of the modeling for computational reasons. Visser (2008) demonstrated that it is a reasonable assumption for individual oaths, and seismic anisotropy can be estimated at a later stage. As in Xu and Beghein (2019), the V_S profile is parameterized with a variable number of interpolation points. The vertical position of these points is the depth at which V_S is perturbed and their horizontal position is the amount by which V_S is perturbed relative to the reference model within a velocity prior. Here the prior for V_S is 10 per cent of the velocity in the reference model at a given depth. While in theory, all parameters (V_S, V_P, ρ, and d) could be perturbed independently, surface waves typically can only resolved V_S due to the existence of strong trade-offs between model parameters. Because of this and to reduce computational costs, we scaled δV_P and $\delta\rho$ to δV_S using $\delta \ln V_P = m_\alpha \delta \ln V_S$ and $\delta \ln \rho = m_\rho \delta \ln V_S$. For the P-wave scaling, we used a linearly varying scaling relation with $m_\alpha = 0.8$ at the surface and $m_\alpha = 0.565$ at 800 km depth (Montagner and Nataf, 1986). For the density scaling, we used $m_\rho = 0.3$ (Anderson et al., 1968). Many studies have demonstrated that these choices do not affect the V_S models (e.g., Panning and Romanowicz, 2006; Beghein, 2010), and Visser (2008) showed that P-wave velocity and density have little influence on the phase velocity perturbation in the frequency range considered (5—20 mHz). Meier et al. (2009) also showed that higher modes cannot resolve perturbations in the depth of deep mantle discontinuities. We thus opted to neglect perturbations in d except for the Moho which was allowed to vary by ± 2 km at each iteration.

In order for the MCMC sampling algorithm to converge within a reasonable amount of time, to reduce the errors introduced by the linearization of the forward modeling, and to avoid cycle skipping, our waveform inversion technique requires a good 1-D reference model. In addition, it has been shown that the Moho depth can have non-linear effects on waveform modeling and phase velocity calculations (Montagner and Jobert, 1988). It is thus preferable for the reference model to have a crust that is representative of the (path-averaged) regional crust rather than using a 1-D globe average such as the Preliminary Reference Earth Model (PREM, Dziewonski and Anderson (1981)) for instance. For each event-station pair, we thus calculated a path-averaged reference model using CRUST1.0 (Laske et al., 2013) and 3-D global model 3D2018_08Sv (Debayle et al., 2016), and computed the corresponding shear-wave sensitivity kernels. While there exist more recent, region-specific crustal models (e.g. Chaput et al. (2014); An et al. (2015b)), their Moho depths only differ significantly from CRUST1.0 (around 40 km) in relatively small, localized areas compared to the length of our ray paths and the long wavelengths of our data: An et al. (2015b) report 55 — 60 km at the GSM, $\sim$50 km along the EANT Mountain Ranges, and around 30 km in northern WANT and 20 — 25 km in southern WANT. In addition, many of our paths sample even greater changes in crustal thickness since they traverse the thin oceanic crust (with a Moho depth close to 5 km), which is well approximated by CRUST1.0, in addition to the thicker continental crust. This, in addition to the fact that the algorithm iteratively modifies the crust and mantle models, means that the path-average model calculated using CRUST1.0 and 3D2018 is a good representation of the average structure and serves our purpose.

The rj-MCMC scheme employed here performs a guided Monte Carlo sampling of the model space using the misfit between the real and the synthetic seismograms. As explained in Xu and Beghein (2019), the method fits seismic waveforms in multiple frequency-time windows, which are chosen using group velocities and S- or SS-wave arrival times such that they include the fundamental and several higher modes. The criteria used to select those windows are summarized in Tab. 1. The synthetic waveforms and the recorded waveforms were compared in those windows and the total misfit function is given by:

$$\text{Misfit}(\mathbf{m}) = \sum_{\mathbf{j=0}}^{\mathbf{M}} \frac{\sum_{\mathbf{i=0}}^{\mathbf{N_j}} (\mathbf{d_{j,i}} - \mathbf{s_{j,i}})^{\mathbf{2}}}{\sum_{\mathbf{i=0}}^{\mathbf{N_j}} \mathbf{d_{j,i}^2}} \tag{4}$$

where $\mathbf{m}$ is the model vector, and $\mathbf{d}$ and $\mathbf{s}$ denote the recorded waveform and synthetic waveform, respectively. M is the number of frequency-time windows while N is the respective number of data points within each window. The normalization factor in the denominator guarantees that the misfits are independent of the absolute amplitudes of earthquakes and are used here for easier quality control. In this study, we sampled a total of 480,000 models and used an ensemble of 1,600 models after the burn-in period for each event-station pair. Examples of waveform fit are shown in Fig. 4.

3.2 Inversions

At each depth z, the path-averaged wave slowness along great circle path l can be expressed as the integral of the local slowness along the great circle path:

$$\frac{1}{V_l(z)} = \frac{1}{d_l} \int_l \frac{1}{V(z,l)} dl, \tag{5}$$

where d_l denotes the epicentral distance for path l and $V_l(z)$ is the wave speed along the path. We applied our MCMC method to each of the 2,000 paths that passed the above-described quality control, resulting in 1,600 velocity profiles $V_l(z)$ for each event-station pair after the burn-in period. We used the mean and standard deviation of these 1,600 velocity profiles to build a 3-D azimuthally anisotropic velocity model as described below.

In a slightly anisotropic medium, the azimuthal variation of SV-wave propagating horizontally with velocity V_{SV} can be expressed as (Montagner and Nataf, 1986):

$$V_{SV}(z,\Psi) = V_0(z) + A_1(z)cos(2\Psi) + A_2(z)sin(2\Psi) + B_1(z)cos(4\Psi) + B_2(z)sin(4\Psi) \tag{6}$$

where Ψ denotes the propagation azimuth. We inverted our ensemble of path-averaged velocities $V_{SV}(z,\Psi)$ at selected depths using a LSQR procedure (Paige and Saunders, 1982) to obtain the isotropic shear-wave velocity $V_0(z)$ and the anisotropic terms $A_1(z)$, $A_2(z)$, $B_1(z)$, and $B_2(z)$. We parameterized the study area with a 2-D triangular grid at each depth, and each $V_{SV}(z,\Psi)$ was weighted using their standard deviation at depth z. In general, the velocity uncertainties increase with depth due to the lower sensitivity of our data set to deeper structure. For instance, most paths have uncertainties smaller than 40 m/s at 60 km and 150 km, but at 600 km the majority of the uncertainties fall in bins larger than 50 m/s (Fig. 5). Shen et al. (2018) reported a standard deviation of 50 — 65 m/s from their Bayesian inversion on fundamental surface waves and receiver functions, which are roughly consistent with our path-specific uncertainties above 250 km.

Regularization is needed in order to solve this ill-posed geophysical problem and to avoid over-fitting the data.

We chose to minimize the following cost function:

$$C = \lambda_1 ||\mathbf{Lm}|| + \lambda_\mathbf{2} ||\mathbf{m}|| \tag{7}$$

where $\mathbf{L}$ is a smoothing operator that acts upon the model vector, $||\mathbf{m}||$ is a L_2-norm term that affects the strength of the velocity anomalies, and λ_1 and λ_2 are tuning parameters. Separate tuning parameters were introduced for the isotropic terms, the 2Ψ terms, and the 4Ψ terms. For each parameter, we used the L-curve method (Hansen, 1998) to select the amount of damping. The preferred damping is chosen at the "elbow" of the L-curve, which represents a good trade-off between variance reduction and model complexity. Different depths were treated independently, and at each depth we started by selecting the damping for the isotropic term. After the optimal regularization is selected for the isotropic term, we proceeded with the L-curve for the 2Ψ terms, and finally with the 4Ψ terms. Fig. 6 shows an example of damping selection at 150 km depth. The significance of the 2Ψ and 4Ψ terms is determined using F-tests (Bevington and Robinson, 2002) and is discussed in the Results section.

4 Results

4.1 Significance of the Anisotropy

As shown in Fig. 6, the variance reduction increases as more parameters are included in the inversion. However, this misfit improvement may be due to the increase in the number of unknowns and may not necessarily be required by the data. In order to test if the anisotropic terms are statistically significant, we performed F-tests (Bevington and Robinson, 2002) following Trampert and Woodhouse (2003).

For this purpose, we defined a reduced χ^2:

$$\chi^2 = \frac{1}{N-M}(\mathbf{d} - \mathbf{Gm})\mathbf{C_d}^{\mathbf{-1}}(\mathbf{d} - \mathbf{Gm}) \tag{8}$$

where $\mathbf{d}$ is the data vector and $\mathbf{G}$ is a matrix describing the relationships between the data and the model parameters. $\mathbf{C_d}$ is the data covariance matrix, which in our case is a diagonal matrix containing the standard deviations of the models shown in Fig. 5. N is the number of data points and M is the trace of the resolution matrix $\mathbf{R}$, i.e. the number of independent parameters for the chosen regularization. The resolution matrix, and thus M, cannot be directly calculated with the LSQR method. Instead, we calculated it by inverting each column of matrix $\mathbf{G}$:

$$\mathbf{R_j} = \mathbf{LG_j} \tag{9}$$

where $\mathbf{L}$ represents the LSQR operator and $\mathbf{R}_j$ is the j-th column of the resolution matrix. Fig. 7 shows an example of reduced χ^2 at 150 km depth as a function of the trace of the resolution matrix. It demonstrates that the reduced χ^2 decreases as the number of independent parameters increases.

To determine whether the reduction in misfit is significant at each depth, we then performed F-tests and compared the preferred models selected by the L-curve method. In such comparisons, the null hypothesis is that the simpler model and the more complicated model can explain the data equivalently well. The F-test calculates the confidence level at which the null hypothesis can be rejected (i.e., the model with more parameters significantly improves the data fit). Here, we set the confidence level threshold at 85% and found that the misfit reduction between the isotropic inversions and isotropic + 2Ψ inversions are only significant at a depth shallower than 300 km, whereas the misfit reduction between the 2Ψ inversions and the 4Ψ inversions is not significant except at a depth of 60 km. Details of the F-test analysis can be found in Tab. 2. Based on these results, we argue that the presence of the 2Ψ azimuthal anisotropic terms is required by the data in the upper mantle above 300 km, but that the 4Ψ terms are generally not needed. This is consistent with the fact that Rayleigh waves are mostly sensitive to the elastic parameters governing the speed of vertically polarized shear waves, which can be inverted from the 2Ψ coefficients $A_1(z)$ and $A_2(z)$ (Montagner and Nataf, 1986). The 4Ψ coefficients $B_1(z)$ and $B_2(z)$ can be seen as depth integrals of the elastic parameters governing the speed of horizontally polarized shear waves instead (e.g. Yuan and Beghein (2014)). We thus focus our discussion on the isotropic model and the 2Ψ anisotropy.

4.2 Isotropic Model

The isotropic part of our 3-D model is displayed in Fig. 8. Because we used data at periods of 50 s and larger, we do not expect the top 50 km to be well constrained, and thus only present the velocity model below that depth. The dichotomy between EANT and WANT dominates the velocity variations at depths of 60 km, 100 km, and 200 km, which indicates distinct seismic patterns underneath the cratonic EANT and the extensional WARS. The largest amplitude anomalies range from +7% relative to PREM (Dziewonski and Anderson, 1981) underneath EANT to about -5% below WANT. Such strong anomalies start to diminish below 200 km, and at MTZ depths the anomalies are generally within +/- 2%.

Vertical slices of three transects are shown in Fig. 9. Transect A — A' samples both WANT and EANT and shows the clear dichotomy between the two regions with relatively slow shear waves under WANT and relatively fast shear waves under EANT. The negative velocity anomalies under WANT are located between about 80 km and 200 km depth and have a relative amplitude of around 4%. The fast velocity anomalies under EANT extend down to 225 km under the GSM with relative amplitudes as high as 7%, but only extend down to about 150 km toward Dronning Maud Land (DML) in the northeastern part of the grid. Profile B — B' crosses EANT from grid North to grid South and shows similar results: the GSM is characterized by the deepest positive anomalies and the fastest wave speeds whereas the anomalies near the coast are of shallower origin. Profile C — C' samples WANT and features negative velocity anomalies. They extend down to 200 km depth beneath MBL and along the Amundsen Sea coast to the Antarctica Peninsula.

4.3 Azimuthal Anisotropy

Fig. 10 represents the 2Ψ anisotropy at depths of 75 km, 150 km, 225 km, and 285 km, superimposed to the APM based on model NUVEL-1A in the no-net rotation reference frame (Gripp and Gordon, 2002). Stronger azimuthal anisotropy can be observed in the Antarctica interior as well as in WILK at 150 km depth. The amplitude of the anisotropy starts to decrease below 225 km. At 285 km, central Antarctica still has around 1% anisotropy, but everywhere else the amplitude is smaller. This is consistent with our F-tests that showed that the 2Ψ terms are not significant below $\sim$300 km.

Abrupt changes in fast directions can also be identified in all four depth slices between WANT and EANT: while the fast seismic axis is roughly subparallel to the APM just east of the TAMs down to 225 km, it is approximately NE-SW west of the TAMs at 75 km and it shows strong lateral variations at 150 km and 225 km depth.

Depth changes are also observed. Note that because the anisotropy amplitude at 285 km is very small, we do not discuss its direction at that depth as it may not be resolved. In WANT, where the APM is oriented grid NW-SE, the fast direction on land near the Amundsen Sea changes from grid NE-SW at 75 km to NW-SE at 150 km depth and changes back to NE-SW at greater depths. While this could be due to vertical trade-offs among model parameters, we consider it unlikely because the sensitivity of the data does not strongly vary laterally at those depths. In EANT, the fast directions of anisotropy show a grid NW-SE dominant direction in the south, roughly following the APM direction at 75 km depth. The fast direction in central and northern EANT rotates from grid NE-SW at 75 km to grid NNW-SSE at larger depths, which also roughly coincides with the APM direction. At 225 km, the fast direction in northern EANT changes again but less so in the southern part of EANT. It should be noted that the edges of EANT, especially the NE grid corner, do not have good azimuthal ray coverage due to the lack of stations. The azimuthal anisotropy in these areas may thus be less reliable compared to regions such as WANT and the center of EANT, which have better azimuthal coverage.

4.4 Synthetic Tests

We implemented synthetic tests to assess the quality of the data coverage and the trade-offs between isotropic and anisotropic model parameters. Fig. 11 shows the tests performed at a depth of 150 km, including an isotropic checkerboard test, an anisotropic (2Ψ) inversion of an isotropic true model, and an anisotropic inversion of an anisotropic true model. Fig. 12 shows an isotropic checkerboard test at 250 km depth.

In the checkerboard test of Fig. 11, the positive and negative anomalies within -70 degrees can be resolved, though some smoothing effects are seen. The resolution in the surrounding oceans is worse than in the continent due to differences in ray path coverage.

In the second test (Fig. 11), small ($< 0.2\%$) anisotropy is visible in the output model, resulting from trade-offs between isotropic and anisotropic parameters. At the transition area between the positive anomalies in EANT and the negative anomalies in WANT, the output anisotropy amplitude reaches 0.6%. Because this amount of anisotropy is much smaller than the anisotropy retrieved from the real data inversion, we argue that the majority of the azimuthal anisotropy in our model comes from the data rather than from trade-off effects.

The recovered amplitude and fast directions in the third test are consistent with the input model over most of the Antarctica continent. Inconsistencies are nevertheless visible in some of the surrounding oceans where the azimuthal coverage is not sufficient. We also note that the isotropic terms in the second and third tests are recovered well, and the amplitudes of the isotropic terms are not significantly affected by the introduction of the anisotropy.

Fig. 12 shows that at 250 km, the input model recovery is less good than at shallower depths. The center anomaly is visible in the output model but with much lower amplitudes. The anomalies around it are smeared out.

5 Discussion

5.1 Isotropic Structure and Lithosphere-Asthenosphere Boundary

Lloyd et al. (2020) identified a negative anomaly extending into the MTZ under MBL, which they associated with a potential mantle plume. We also observe negative velocity anomalies underneath MBL. However, while they are visible in the upper 200 km and between 300 km and 400 km depth, they are almost non-existent between 200 km and 300 km, questioning whether they are part of the same vertical structure. In addition, the lateral spread of these anomalies is large (close to 1500 km), likely because the long wavelength of the surface waves (especially of the higher modes) limits the horizontal resolution of the 3-D model at those depths. It is therefore difficult to confidently conclude that we see the signature of a plume based on our model. In general, our isotropic velocity anomalies are the strongest above 200 km depth, below which they start to decrease down to +/- 2% at MTZ depths. Just like for the plume hypothesis, we refrain from interpreting these MTZ anomalies because of the limited resolution at these depths. Indeed, as shown in Fig. 5, the uncertainties of the path-specific measurements increase with depth while the amplitude of the velocity anomalies decreases. The deeper anomalies are thus less well resolved than the shallower ones.

The isotropic part of our velocity maps shows strong positive anomalies (up to 7%) in EANT extending down to about 225 km under the GSM. On the contrary, they only extend down to about 150 km near DML in the northeastern part of the grid. These results are consistent with Heeszel et al. (2013) and Lloyd et al. (2020) in that both the thickest part of the craton and the fastest wave speed are located under the GSM and the thinnest parts can be found near the coast.

Different proxies can be used to approximate the lithosphere-asthenosphere boundary (LAB) depth. If we use the depth extent of the relatively fast velocity anomalies, our results suggest a thinner lithosphere closer to the coast than in central EANT. It also results in LAB depths consistent with those of Ritzwoller et al. (2001) and Danesi and Morelli (2001) but shallower than in Lloyd et al. (2020) or Heeszel et al. (2013). However, the choice of the velocity contour to determine the depth extent of the positive V_{SV} anomalies is subjective and depends on the amount of regularization applied. Following Bartzsch et al. (2011), we instead approximated the LAB depth as the middle of the interval over which V_{SV} decreases in our isotropic model. Fig. 13 shows the resulting LAB depth for the Antarctic Plate. It demonstrates a clear difference between WANT and EANT with a LAB depth of around 80 km for WANT and around 180 km for central EANT. The estimated values for WANT are in agreement with the 70 — 100 km range obtained by Heeszel et al. (2016). Compared to An et al. (2015a), who defined the LAB as the shallowest position with a temperature crossing the 1330° adiabat, we find a shallower LAB in the center of EANT (around 190 km compared to their 225 km). The difference is likely caused by the different definitions of the LAB and the lower horizontal resolution of our isotropic model due to the use of surface waves and higher modes at longer periods.

5.2 Anisotropy and Cratonic Layering

Global-scale azimuthal anisotropy models resulting from surface wave inversions usually display a good correlation between the fast seismic direction and APM models in regions with a simple tectonic history, such as the asthenosphere under oceanic plates (Beghein et al., 2014). In regions with a complicated tectonic history, such as continents, this correlation can be low (Debayle and Ricard, 2013). In addition, the Antarctic continent moves slowly with respect to whole mantle plate motion models (Gripp and Gordon, 2002) and SKS splitting measurements are generally inconsistent with the APM in both the hotspot and the no-net rotation (NNR) reference frames (Accardo et al., 2014). The observed anisotropic fabric is therefore unlikely to result from shear associated with the viscous drag of the Antarctic lithosphere over the asthenosphere. However, the lack of vertical resolution of SKS measurements can cast some doubts on such inferences. Our 3-D anisotropy model is better suited to examine the relation between seismic anisotropy and APM. In Fig. 10, we plotted the APM based on model NUVEL-1A (DeMets et al., 1994) in the NNR reference frame superimposed to the fast seismic wave directions from our model. We first discuss WANT and then EANT.

Over most of WANT, the APM direction is at an angle with the fast seismic directions of our model. Around MBL and the Ellsworth–Whitmore Mountains, the fast directions are dominantly Grid SW — NE at depths shallower than 100 km. At 150 km, east of MBL, the seismic fast directions rotate and align better with the APM in the MBL area. This may imply, contrary to conclusions based on SKS splitting, that the fast direction between 100 — 150 km indicates olivine LPO due to present-day mantle deformation within the asthenosphere, whereas the azimuthal anisotropy at shallower depth mainly reflects extensive Cenozoic extension including the final pulse of western WARS rifting in the Miocene (Accardo et al., 2014). At greater depths, the fast direction in WANT changes again and does not reflect the APM direction. We refrain, however, to interpret the depth changes in anisotropy in this part of Antarctica because WANT is relatively small compared to EANT and WANT anisotropy may suffer from smoothing and from the lateral resolution of our data.

For EANT, the fast directions do not match the APM at 75 km and may reflect frozen-in anisotropy within the shallow lithosphere. On the contrary, at 150 km depth and 225 km depth, the fast seismic directions are roughly subparallel to the APM. This is, however, likely too shallow to reflect asthenospheric present-day deformation since the estimated LAB depth for the East Antarctica Craton is around 200 km under the GSM (Fig. 13) and possibly deeper (Lloyd et al., 2020). We propose that this change in fast directions between 75 km and 150 km depth indicates the presence of a second layer in the thick cratonic lithosphere. Similar changes with depth of the fast axis direction of azimuthal anisotropy have been observed within other cratons (e.g., North American craton (Snyder and Bruneton, 2007; Yuan and Romanowicz, 2010; Yuan et al., 2011) and sometimes coincide with the depth of seismic discontinuities (e.g., Foster et al., 2014; Bodin et al., 2016). Depth variations in anisotropic properties have also been reported by authors using anisotropic receiver function analyses in Australia (Wirth and Long, 2014; Chen et al., 2021; Birkey and Ford, 2023). These changes coincide with seismic discontinuities and reveal the presence of layers within the cratonic lithosphere (e.g., Foster et al., 2014; Bodin et al., 2016). This layering likely reflects tectonic events related to the assembly and evolution of the craton.

5.3 Comparison with SKS Splitting

The observation of shear-wave splitting is a direct indication of seismic anisotropy along the path taken by the phase considered (see review by Savage (1999)). It can thus be useful, though not straightforward, to predict shear-wave splitting delay times and fast directions from our 3-D model and compare them with measurements. Montagner et al. (2000) showed that a 3-D azimuthally anisotropic model can be used to predict SKS delay times δt and their fast directions Ψ under the assumption of weak anisotropy with a horizontal axis of symmetry:

$$\delta t = \sqrt{\left(\int_0^R \frac{G_s}{V_{SV}L}dr\right)^2 + \left(\int_0^R \frac{G_c}{V_{SV}L}dr\right)^2} \tag{10}$$

and

$$\tan 2\Psi = \frac{\int_0^R \frac{G_s}{V_{SV}L}dr}{\int_0^R \frac{G_c}{V_{SV}L}dr} \tag{11}$$

where R is the planet's radius, and $L = V_{SV}^2/\rho$ is the Love elastic parameter of the isotropic model. G_c and G_s are the 2Ψ elastic parameters that govern the azimuthal anisotropy amplitude $G = \sqrt{G_s^2 + G_c^2}$ and fast direction $\Theta = \frac{1}{2}\arctan\left(G_s/G_c\right)$ of SV waves. Although comparing predictions from a long-wavelength surface wave model with measurements from body waves is not straightforward due to their different vertical and horizontal resolutions, it can sometimes inform us about the depth of origin of the measured shear-wave splitting.

We calculated the predicted SKS splitting delay times and fast directions using the above two equations and our azimuthally anisotropic model between depths of 60 km and 300 km, where the anisotropy was shown to be required by our data. The predictions shown in Fig. 14 are compared with previous SKS splitting measurements in Antarctica (Müller, 2001; Pondrelli et al., 2006; Bayer et al., 2007; Reading and Heintz, 2008; Barklage et al., 2009; Hernandez et al., 2009; Salimbeni et al., 2010; Accardo et al., 2014; Graw and Hansen, 2017; Lucas et al., 2022). We note that we only plotted available SKS measurements with good quality from these previous studies and that some of SKS measurements present large uncertainties in both SKS delay time amplitudes and fast directions. The thick black bar located at the GSM represents the overall splitting directions from Hernandez et al. (2009).

Overall, our predicted splitting times roughly agree with the observations in WANT with a dominant fast splitting direction grid SW — NE at EWM, WARS, and MBL. Since the wave fast direction of our model changes from grid SW — NE in the top 150 km to NW — SE at greater depths (Fig. 10), this indicates that the shear-wave splitting direction in WANT is dominated by anisotropy in the top 150 km of the mantle. In EANT, differences between SKS data and predictions vary more. Measurements by Accardo et al. (2014) at stations located in the DML show good agreement with our predictions, but measurements by Müller (2001) in that same region differ. At the GSM, the observations are quasi-perpendicular to our predictions. Our predictions in Victoria Land are oriented grid NNW — SSE. Measurements in this area present a lot of scatter and differences between studies. However, the general trend of the data in northern Victoria Land is that the fast axis is grid NNE — SSW. In the southern part of the region, three measurements by Pondrelli et al. (2006) are in closer agreement with our model predictions, but this is an area where our azimuthal coverage is lower and the azimuthal anisotropy may not be resolved. These discrepancies between predictions and measurements in EANT are likely due in part to differences in lateral resolution, but they may also point to deeper anisotropy than our higher modes were able to detect and/or a crustal origin that we cannot resolve at the periods analyzed. Zhou et al. (2023) showed indeed that azimuthal anisotropy is present in the crust, though they found that its amplitude was relatively small. It may also indicate that the depth dependence of the anisotropy in EANT is even more complex than can be resolved with the present data and higher resolution models will be needed to reconcile the data sets.

6 Conclusions

We obtained a new three-dimensional model of shear-wave velocity and azimuthal anisotropy in the upper mantle and mantle transition zone under Antarctica. Our velocity model shows a clear east-west dichotomy with velocities faster than average down to at least 200 km in EANT and generally lower than average in WANT. In particular, the Marie Bird Land, which is located in the more tectonically active WANT and is associated with recent volcanism, is characterized by negative velocity anomalies down to about 400 km depth. This signal could thus be related to the presence of a plume, as suggested by other authors. However, while we found negative velocity perturbations between 50 km and 200 km as well as between 300 km and 400 km, it is unclear whether the two anomalies are connected and we thus cannot conclude regarding the existence of a plume with our data set. Using our velocity profiles to estimate the LAB depth, we estimate that the cratonic root is about 200 km thick and the LAB depth in the younger WANT is around 80 km.

We found significant azimuthal anisotropy in the top 300 km under the Antarctica continent and an abrupt change in the fast seismic wave direction was detected between East and West Antarctica, similar to the east-west dichotomy seen in the isotropic part of the model. The anisotropy amplitude is the strongest between 100 km and 200 km depth under East Antarctica, and depth changes in fast direction are observed within the craton. This suggests layering within the stable, old lithosphere, as seen in other regions of the world, and may reflect the history of formation of the craton.

Our model also enabled us to give new context to the origin of past shear-wave splitting measurements. Shear-wave splitting delay time predictions based on our anisotropy model show good agreement with observations in WANT where the dominant fast splitting direction is grid SW - NE. Considering that the anisotropy fast axis changes in our model from grid SW - NE in the top 150 km to roughly NW-SE at greater depths, this indicates that the shear-wave splitting direction in WANT is dominated by anisotropy in the top 150 km of the mantle. In EANT, however, less agreement between data and predictions was found, possibly indicating a more complex 3-D anisotropy than in WANT, associated with different stages of deformation during the assembly of the craton.

Acknowledgements

H.X. developed and ran the codes to perform the inversions, edited the manuscript, and made the figures. C.B. wrote and edited the manuscript, updated the figures, and managed the project.

Data and code availability

The data used in this study are available on the IRIS DMC.

Competing interests

The authors do not have any competing interests, financial or otherwise.

References

Accardo, N. J., Wiens, D. A., Hernandez, S., Aster, R. C., Nyblade, A., Huerta, A., Anandakrishnan, S., Wilson, T., Heeszel, D. S., and Dalziel, I. W. Upper mantle seismic anisotropy beneath the West Antarctic Rift System and surrounding region from shear wave splitting analysis. *Geophys. J. Int.*, 198(1):414–429, 2014. doi: 10.1093/gji/ggu117.

Alex Brisbourne, Graham Stuart, and John Paul O'Donnell. UKANET: UK Antarctic Network, 2016.

An, M., Wiens, D. A., Zhao, Y., Feng, M., Nyblade, A., Kanao, M., Li, Y., Maggi, A., and Lévêque, J.-J. Temperature, lithosphere-asthenosphere boundary, and heat flux beneath the Antarctic Plate inferred from seismic velocities. *J. Geophys. Res.: Solid Earth*, 120(12):8720–8742, 2015a. doi: 10.1002/2014JB011332.

An, M., Wiens, D. A., Zhao, Y., Feng, M., Nyblade, A. A., Kanao, M., Li, Y., Maggi, A., and Lévêque, J.-J. S-velocity model and inferred Moho topography beneath the Antarctic Plate from Rayleigh waves. *J. Geophys. Res.: Solid Earth*, 120(1):359–383, 2015b. doi: 10.1002/2014JB011332.

Anandakrishnan, S. and Wiens, D. A Broadband Seismic Investigation of Deep Continental Structure Across the East-West Antarctic Boundary, 2000.

Anderson, D. L. Love Wave Dispersion in Heterogeneous Anisotropic Media. *Geophysics*, 27:445–454, 1962. doi: 10.1190/1.1439042.

Anderson, J. B. *Antarctic marine geology*. Cambridge University Press, 1999. doi: 10.1017/CBO9780511759376.

Anderson, O. L., Schreiber, E., Liebermann, R. C., and Soga, N. Some elastic constant data on minerals relevant to geophysics. *Reviews of Geophysics*, 6(4):491–524, 1968.

Auer, L., Boschi, L., Becker, T. W., Nissen-Meyer, T., and Giardini, D. Savani: A variable resolution whole-mantle model of anisotropic shear velocity variations based on multiple data sets. *J. Geophys. Res.: Solid Earth*, 119(4):3006 – 3034, 2014. doi: 10.1002/2013jb010773.

Barklage, M., Wiens, D. A., Nyblade, A., and Anandakrishnan, S. Upper mantle seismic anisotropy of South Victoria Land and the Ross Sea coast, Antarctica from SKS and SKKS splitting analysis. *Geophys. J. Int.*, 178(2):729–741, 2009. doi: 10.1111/j.1365-246X.2009.04158.x.

Barruol, G. and Hoffmann, R. Upper mantle anisotropy beneath the Geoscope stations. *J. Geophys. Res.: Solid Earth*, 104(B5):10757–10773, 1999. doi: 10.1029/1999JB900033.

Bartzsch, S., Lebedev, S., and Meier, T. Resolving the lithosphere–asthenosphere boundary with seismic Rayleigh waves. *Geophysical Journal International*, 186(3):1152–1164, 2011.

Bayer, B., Müller, C., Eaton, D. W., and Jokat, W. Seismic anisotropy beneath Dronning Maud Land, Antarctica, revealed by shear wave splitting. *Geophys. J. Int.*, 171(1):339–351, 2007. doi: 10.1111/j.1365-246X.2007.03519.x.

Becker, T. W., Kellogg, J. B., Ekström, G., and O'Connell, R. J. Comparison of azimuthal seismic anisotropy from surface waves and finite strain from global mantle-circulation models. *Geophys. J. Int.*, 155(2):696 – 714, 2003. doi: 10.1046/j.1365-246x.2003.02085.x.

Beghein, C. Radial anisotropy and prior petrological constraints: A comparative study. *Journal of Geophysical Research*, 115(B03303), 2010. doi: 10.1029/2008jb005842.

Beghein, C., Yuan, K., Xing, Z., and Schmerr, N. Changes in Seismic Anisotropy Shed Light on the Nature of the Gutenberg Discontinuity. *Science*, 343(6176):1237 – 1240, 2014. doi: 10.1126/science.1246724.

Behrendt, J. C. Crustal and lithospheric structure of the West Antarctic Rift System from geophysical investigations—a review. *Global and Planetary Change*, 23(1-4):25–44, 1999.

Behrendt, J. C., LeMasurier, W. E., Cooper, A. K., Tessensohn, F., Tréhu, A., and Damaske, D. Geophysical studies of the West Antarctic Rift System. *Tectonics*, 10(6):1257–1273, 1991. doi: 10.1029/91tc00868.

Beucler, E., Stutzmann, E., and Montagner, J.-P. Surface wave higher-mode phase velocity measurements using a roller-coaster-type algorithm. *Geophys. J. Int.*, 155(1):289–307, 2003. doi: 10.1046/j.1365-246X.2003.02041.x.

Bevington, P. and Robinson, K. *Data Reduction and Error Analysis for the Physical Sciences*. McGraw-Hill, New York, N. Y., 3rd edition, 2002.

Birkey, A. and Ford, H. A. Anisotropic structure of the Australian continent. *Frontiers in Earth Science*, 10:1055480, 2023. doi: 10.3389/feart.2022.1055480.

Block, A. E., Bell, R. E., and Studinger, M. Antarctic crustal thickness from satellite gravity: Implications for the Transantarctic and Gamburtsev Subglacial Mountains. *Earth Planet. Sci. Lett.*, 288(1-2):194–203, 2009. doi: 10.1016/j.epsl.2009.09.022.

Bodin, T. and Sambridge, M. Seismic tomography with the reversible jump algorithm. *Geophysical Journal International*, 178(3):1411–1436, 2009.

Bodin, T., Sambridge, M., Tkalčić, H., Arroucau, P., Gallagher, K., and Rawlinson, N. Transdimensional inversion of receiver functions and surface wave dispersion. *Journal of Geophysical Research: Solid Earth*, 117(B2), 2012.

Bodin, T., Leiva, J., Romanowicz, B., Maupin, V., and Yuan, H. Imaging anisotropic layering with Bayesian inversion of multiple data types. *Geophysical Journal of the Royal Astronomical Society*, 206(1):605 – 629, 2016. doi: 10.1093/gji/ggw124.

Boger, S. D. Antarctica — Before and after Gondwana. *Gondwana Research*, 19(2):335–371, 2011. doi: https://doi.org/10.1016/j.gr.2010.09.003.

Chaput, J., Aster, R. C., Huerta, A., Sun, X., Lloyd, A., Wiens, D., Nyblade, A., Anandakrishnan, S., Winberry, J. P., and Wilson, T. The crustal thickness of West Antarctica. *J. Geophys. Res.: Solid Earth*, 119(1):378–395, 2014. doi: 10.1002/2013JB010642.

Chen, X., Levin, V., Yuan, H., Klaser, M., and Li, Y. Seismic Anisotropic Layering in the Yilgarn and Superior Cratonic Lithosphere. *Journal of Geophysical Research: Solid Earth*, 126(8):e2020JB021575, 2021. doi: 10.1029/2020JB021575.

Dahlen, F. The Normal Modes of a Rotating, Elliptical Earth. *Geophysical Journal of the Royal Astronomical Society*, 16(4):329 – 367, 1968. doi: 10.1111/j.1365-246x.1968.tb00229.x.

Dalziel, I. W. D. Antarctica; a tale of two supercontinents? *Annu. Rev. Earth Planet. Sci.*, 20(1):501–526, 1992. doi: 10.1146/annurev.ea.20.050192.002441.

Danesi, S. and Morelli, A. Group velocity of Rayleigh waves in the Antarctic region. *Physics of the Earth and Planetary Interiors*, 122(1-2):55–66, 2000. doi: 10.1016/s0031-9201(00)00186-2.

Danesi, S. and Morelli, A. Structure of the upper mantle under the Antarctic Plate from surface wave tomography. *Geophys. Res. Lett.*, 28 (23):4395–4398, 2001. doi: 10.1029/2001GL013431.

Debayle, E. and Ricard, Y. Seismic observations of large-scale deformation at the bottom of fast-moving plates. *Earth and Planetary Science Letters*, 376:165–177, 2013.

Debayle, E., Dubuffet, F., and Durand, S. An automatically updated S-wave model of the upper mantle and the depth extent of azimuthal anisotropy. *Geophysical Research Letters*, 43(2):674–682, 2016.

DeMets, C., Gordon, R. G., Argus, D. F., and Stein, S. Effect of recent revisions to the geomagnetic reversal time scale on estimates of current plate motions. *Geophys. Res. Lett.*, 21(20):2191–2194, 1994. doi: 10.1029/94GL02118.

Dewart, G. and Toksöz, M. N. Crustal Structure in East Antarctica from Surface Wave Dispersion. *Geophys. J. Int.*, 10(2):127–139, 1965. doi: 10.1111/j.1365-246X.1965.tb03056.x.

Dziewonski, A. and Anderson, D. Preliminary reference Earth model. *Phys. Earth Planet. Inter.*, 25(4):297–356, 1981. doi: 10.1016/0031-9201(81)90046-7.

Dziewonski, A. M., Chou, T.-A., and Woodhouse, J. H. Determination of earthquake source parameters from waveform data for studies of global and regional seismicity. *J. Geophys. Res.: Solid Earth*, 86(B4):2825–2852, 1981. doi: 10.1029/JB086iB04p02825.

Ebbing, J., Dilixiati, Y., and Haas, P. e. a. East Antarctica magnetically linked to its ancient neighbours. *Scientific Reports*, 11(5513), 2021. doi: 10.1038/s41598-021-84834-1.

Ekström, G. and Dziewonski, A. M. The unique anisotropy of the Pacific upper mantle. *Nature*, 394:168 – 172, 07 1998. doi: 10.1038/28148.

Ekström, G., Nettles, M., and Dziewoński, A. M. The global CMT project 2004–2010: Centroid-moment tensors for 13,017 earthquakes. *Phys. Earth Planet. Inter.*, 200-201:1–9, 2012. doi: 10.1016/j.pepi.2012.04.002.

Emry, E., Nyblade, A. A., Julià, J., Anandakrishnan, S., Aster, R., Wiens, D. A., Huerta, A. D., and Wilson, T. J. The mantle transition zone beneath West Antarctica: Seismic evidence for hydration and thermal upwellings. *Geochem. Geophys. Geosystems*, 16(1):40–58, 2015. doi: 10.1002/2014GC005588.

Emry, E. L., Nyblade, A. A., Horton, A., Hansen, S. E., Julià, J., Aster, R. C., Huerta, A. D., Winberry, J. P., Wiens, D. A., and Wilson, T. J. Prominent thermal anomalies in the mantle transition zone beneath the Transantarctic Mountains. *Geology*, 48(7):748–752, 2020. doi: 10.1130/g47346.1.

Evison, F., Ingham, C., Orr, R., and le Fort, J. Thickness of the Earth's crust in Antarctica and the surrounding oceans. *Geophys. J. R. A. S.*, 3 (3):289–306, 1960. doi: 10.1111/j.1365-246X.1960.tb01704.x.

Ferraccioli, F., Finn, C. A., Jordan, T. A., Bell, R. E., Anderson, L. M., and Damaske, D. East Antarctic rifting triggers uplift of the Gamburtsev Mountains. *Nature*, 479(7373):388–392, 2011. doi: 10.1038/nature10566.

Ferreira, A. M., Faccenda, M., Sturgeon, W., Chang, S.-J., and Schardong, L. Ubiquitous lower-mantle anisotropy beneath subduction zones. *Nature Geoscience*, pages 1 – 8, 2019. doi: 10.1038/s41561-019-0325-7.

Finotello, M., Nyblade, A., Julia, J., Wiens, D., and Anandakrishnan, S. Crustal Vp-Vs ratios and thickness for Ross Island and the Transantarctic Mountain front, Antarctica. *Geophys. J. Int.*, 185(1):85–92, 2011. doi: 10.1111/j.1365-246x.2011.04946.x.

Fitzgerald, P. *Tectonics and landscape evolution of the Antarctic plate since Gondwana breakup, with an emphasis on the West Antarctic rift system and the Transantarctic Mountains*, volume 35, pages 453–469. The Royal Society of New Zealand, New Zealand, 2002.

Foster, K., Dueker, K., Schmandt, B., and Yuan, H. A sharp cratonic lithosphere–asthenosphere boundary beneath the American Midwest and its relation to mantle flow. *Earth and Planetary Science Letters*, 402(C):82 – 89, 2014. doi: 10.1016/j.epsl.2013.11.018.

Fouch, M. J. and Fischer, K. M. Mantle anisotropy beneath northwest Pacific subduction zones. *J. Geophys. Res.: Solid Earth*, 101(B7):15987, 1996. doi: 10.1029/96jb00881.

Granot, R., Cande, S., Stock, J., Davey, F., and Clayton, R. Postspreading rifting in the Adare Basin, Antarctica: regional tectonic consequences. *Geochem. Geophys. Geosystems*, 11(8), 2010. doi: 10.1029/2010GC003105.

Graw, J. H. and Hansen, S. E. Upper mantle seismic anisotropy beneath the Northern Transantarctic Mountains, Antarctica from PKS, SKS, and SKKS splitting analysis. *Geochemistry, Geophysics, Geosystems*, 18(2):544–557, 2017. doi: 10.1002/2016gc006729.

Gripp, A. E. and Gordon, R. G. Young tracks of hotspots and current plate velocities. *Geophys. J. Int.*, 150(2):321–361, 2002.

Gung, Y., Panning, M. P., and Romanowicz, B. Global anisotropy and the thickness of continents. *Nature*, 422(6933):707 – 711, 2003. doi: 10.1038/nature01559.

Hansen, P. C. *Rank-deficient and discrete ill-posed problems: numerical aspects of linear inversion*. SIAM, 1998.

Hansen, S. Transantarctic Mountains Northern Network, 2012.

Hansen, S. E., Julia, J., Nyblade, A. A., Pyle, M. L., Wiens, D. A., and Anandakrishnan, S. Using S wave receiver functions to estimate crustal structure beneath ice sheets: An application to the Transantarctic Mountains and East Antarctic craton. *Geochem. Geophys. Geosystems*, 10(8), 2009. doi: 10.1029/2009GC002576.

Hansen, S. E., Nyblade, A. A., Heeszel, D. S., Wiens, D. A., Shore, P., and Kanao, M. Crustal structure of the Gamburtsev Mountains, East Antarctica, from S-wave receiver functions and Rayleigh wave phase velocities. *Earth Planet. Sci. Lett.*, 300(3-4):395–401, 2010. doi: 10.1016/j.epsl.2010.10.022.

Hansen, S. E., Graw, J. H., Kenyon, L. M., Nyblade, A. A., Wiens, D. A., Aster, R. C., Huerta, A. D., Anandakrishnan, S., and Wilson, T. Imaging the Antarctic mantle using adaptively parameterized P-wave tomography: Evidence for heterogeneous structure beneath West Antarctica. *Earth Planet. Sci. Lett.*, 408:66–78, 2014. doi: 10.1016/j.epsl.2014.09.043.

Heeszel, D. S., Wiens, D. A., Nyblade, A. A., Hansen, S. E., Kanao, M., An, M., and Zhao, Y. Rayleigh wave constraints on the structure and tectonic history of the Gamburtsev Subglacial Mountains, East Antarctica. *J. Geophys. Res.: Solid Earth*, 118(5):2138–2153, 2013. doi: 10.1002/jgrb.50171.

Heeszel, D. S., Wiens, D. A., Anandakrishnan, S., Aster, R. C., Dalziel, I. W. D., Huerta, A. D., Nyblade, A. A., Wilson, T. J., and Winberry, J. P. Upper mantle structure of central and West Antarctica from array analysis of Rayleigh wave phase velocities. *J. Geophys. Res.: Solid Earth*, 121(3):1758–1775, 2016. doi: 10.1002/2015jb012616.

Hernandez, S., Wiens, D., Anandakrishnan, S., Aster, R., Huerta, A., Nyblade, A., and Wilson, T. Seismic anisotropy of the Antarctic upper mantle from shear wave splitting analysis of POLENET and AGAP seismograms. In *AGU Fall Meeting Abstracts*, volume 2009, pages U51C–0043, 2009.

Huang, Q., Schmerr, N., Waszek, L., and Beghein, C. Constraints on Seismic Anisotropy in the Mantle Transition Zone From Long-Period SS Precursors. *J. Geophys. Res.: Solid Earth*, 124(7):6779–6800, 6 2019. doi: 10.1029/2019jb017307.

Jeans, J. H. The propagation of earthquake waves. *Proceedings of the Royal Society of London. Series A, Containing Papers of a Mathematical and Physical Character*, 102(718):554–574, 1923. doi: 10.1098/rspa.1923.0015.

Karato, S.-i. and Wu, P. Rheology of the Upper Mantle - a Synthesis. *Science*, 260(5109):771 – 778, 05 1993. doi: 10.1126/science.260.5109.771.

Karato, S.-i., Jung, H., Katayama, I., Skemer, P., and Skemer, P. Geodynamic Significance of Seismic Anisotropy of the Upper Mantle: New Insights from Laboratory Studies. *Annu. Rev. Earth Planet. Sci.*, 36(1):59 – 95, 2008. doi: 10.1146/annurev.earth.36.031207.124120.

Kovach, R. and Press, F. Surface wave dispersion and crustal structure in Antarctica and the Surrounding Oceans. *Ann. Geophys.*, 14:211–224, 1961. doi: 10.4401/ag-5296.

Laske, G., Masters, G., Ma, Z., and Pasyanos, M. Update on CRUST1. 0—A 1-degree global model of Earth's crust. In *Geophys. res. abstr*, volume 15, page 2658, 2013.

Lawrence, J. F., Wiens, D. A., Nyblade, A. A., Anandakrishnan, S., Shore, P. J., and Voigt, D. Crust and upper mantle structure of the Transantarctic Mountains and surrounding regions from receiver functions, surface waves, and gravity: Implications for uplift models. *Geochem. Geophys. Geosystems*, 7(10):n/a – n/a, 2006. doi: 10.1029/2006gc001282.

Lebedev, S., Nolet, G., Meier, T., and Van der Hilst, R. D. Automated multimode inversion of surface and S waveforms. *Geophys. J. Int.*, 162 (3):951–964, 2005. doi: 10.1111/j.1365-246X.2005.02708.x.

LeMasurier, W. E. and Landis, C. A. Mantle-plume activity recorded by low-relief erosion surfaces in West Antarctica and New Zealand. *GSA Bulletin*, 108(11):1450–1466, 1996. doi: 10.1130/0016-7606(1996)108<1450:mparbl>2.3.co;2.

Lloyd, A., Wiens, D., Zhu, H., Tromp, J., Nyblade, A., Aster, R., Hansen, S., Dalziel, I., Wilson, T., Ivins, E., and O'Donnell, J. P. Seismic structure of the Antarctic upper mantle imaged with adjoint tomography. *J. Geophys. Res.: Solid Earth*, 125(3), 2020. doi: 10.1029/2019JB017823.

Lloyd, A. J., Wiens, D. A., Nyblade, A. A., Anandakrishnan, S., Aster, R. C., Huerta, A. D., Wilson, T. J., Dalziel, I. W., Shore, P. J., and Zhao, D.

A seismic transect across West Antarctica: Evidence for mantle thermal anomalies beneath the Bentley Subglacial Trench and the Marie Byrd Land Dome. *J. Geophys. Res.: Solid Earth*, 120(12):8439–8460, 2015. doi: 10.1002/2015JB012455.

Long, M. D. and van der Hilst, R. D. Upper mantle anisotropy beneath Japan from shear wave splitting. *Phys. Earth Planet. Inter.*, 151(3-4): 206–222, 2005. doi: 10.1016/j.pepi.2005.03.003.

Lucas, E. M., Nyblade, A. A., Accardo, N. J., Lloyd, A. J., Wiens, D. A., Aster, R. C., Wilson, T. J., Dalziel, I. W., Stuart, G. W., O'Donnell, J. P., Winberry, J. P., and Huerta, A. D. Shear Wave Splitting Across Antarctica: Implications for Upper Mantle Seismic Anisotropy. *Journal of Geophysical Research: Solid Earth*, 127(4), 2022. doi: 10.1029/2021jb023325.

Lynner, C. and Long, M. D. Heterogeneous seismic anisotropy in the transition zone and uppermost lower mantle: evidence from South America, Izu-Bonin and Japan. *Geophys. J. R. A. S.*, 201(3):1545 – 1552, 2015. doi: 10.1093/gji/ggv099.

Lynner, C., Lynner, C., and Long, M. D. Lowermost mantle anisotropy and deformation along the boundary of the African LLSVP. *Geophys. Res. Lett.*, 41:3447–3454, 2014. doi: 10.1002/2014gl059875.

Marone, F., Gung, Y., and Romanowicz, B. Three-dimensional radial anisotropic structure of the North American upper mantle from inversion of surface waveform data. *Geophys. J. R. A. S.*, 171(1):206 – 222, 2007. doi: 10.1111/j.1365-246x.2007.03465.x.

Masters, G., Woodhouse, J., and Freeman, G. Mineos v1.0.2 [software], 2011.

Meier, U., Trampert, J., and Curtis, A. Global variations of temperature and water content in the mantle transition zone from higher mode surface waves. *Earth and Planetary Science Letters*, 282(1-4):91 – 101, 2009. doi: 10.1016/j.epsl.2009.03.004.

Montagner, J.-P. and Jobert, N. Vectorial tomography ii. Application to the Indian Ocean. *Geophysical Journal of the Royal Astronomical Society*, 94(2):309–344, 1988. doi: 10.1111/j.1365-246x.1988.tb05904.x.

Montagner, J.-P. and Nataf, H. A Simple Method for Inverting the Azimuthal Anisotropy of Surface-Waves. *J. Geophys. Res.*, 91(B1):511 – 520, 1986. doi: 10.1029/jb091ib01p00511.

Montagner, J. P., Romanowicz, B., and Karczewski, J.-F. A first step toward an oceanic geophysical observatory. *Eos, Transactions American Geophysical Union*, 75(13):150–154, 1994. doi: 10.1029/94EO00848.

Montagner, J.-P., Griot-Pommera, D.-A., and Lavé, J. How to relate body wave and surface wave anisotropy? *Journal of Geophysical Research: Solid Earth*, 105(B8):19015–19027, 2000.

Morelli, A. and Danesi, S. Seismological imaging of the Antarctic continental lithosphere: a review. *Global and Planetary Change*, 42(1): 155–165, 2004. doi: https://doi.org/10.1016/j.gloplacha.2003.12.005.

Müller, C. Upper mantle seismic anisotropy beneath Antarctica and the Scotia Sea region. *Geophys. J. Int.*, 147(1):105–122, 2001. doi: 10.1046/j.1365-246X.2001.00517.x.

O'Donnell, J., Brisbourne, A. M., Stuart, G., Dunham, C., Yang, Y., Nield, G., Whitehouse, P., Nyblade, A., Wiens, D., Anandakrishnan, S., Aster, R. C., Huerta, A. D., Lloyd, A. J., Wilson, T., and Winberry, J. P. Mapping crustal shear wave velocity structure and radial anisotropy beneath West Antarctica using seismic ambient noise. *Geochem. Geophys. Geosystems*, 20(11):5014–5037, 2019. doi: 10.1029/2019GC008459.

Paige, C. C. and Saunders, M. A. LSQR: An algorithm for sparse linear equations and sparse least squares. *ACM Transactions on Mathematical Software (TOMS)*, 8(1):43–71, 1982.

Panning, M. and Romanowicz, B. A three-dimensional radially anisotropic model of shear velocity in the whole mantle. *Geophys. J. Int.*, 167(1):361 – 379, 2006. doi: 10.1111/j.1365-246x.2006.03100.x.

Pondrelli, S. and Azzara, R. Upper mantle anisotropy in Victoria Land (Antarctica). In *Geodynamics of Lithosphere & Earth's Mantle*, pages 433–442. Springer, 1998.

Pondrelli, S., Margheriti, L., and Danesi, S. Antarctica, Contributions to Global Earth Sciences. pages 155–161, 2006. doi: 10.1007/3-540-

32934-x_19.

Press, F. and Gilbert, D. Extent of the Antarctic Continent. *Science*, 129(3347):462–463, 1959. doi: 10.1126/science.129.3347.462.

Pyle, M. L., Wiens, D. A., Nyblade, A. A., and Anandakrishnan, S. Crustal structure of the Transantarctic Mountains near the Ross Sea from ambient seismic noise tomography. *Journal of Geophysical Research: Solid Earth*, 115(B11), 2010. doi: 10.1029/2009jb007081.

Ramirez, C., Nyblade, A., Hansen, S., Wiens, D., Anandakrishnan, S., Aster, R., Huerta, A., Shore, P., and Wilson, T. Crustal and upper-mantle structure beneath ice-covered regions in Antarctica from S-wave receiver functions and implications for heat flow. *Geophysical Journal International*, 204(3):1636–1648, 2016. doi: 10.1093/gji/ggv542.

Ramirez, C., Nyblade, A., Emry, E. L., Julià, J., Sun, X., Anandakrishnan, S., Wiens, D. A., Aster, R. C., Huerta, A. D., Winberry, P., and Wilson, T. Crustal structure of the Transantarctic Mountains, Ellsworth Mountains and Marie Byrd Land, Antarctica: constraints on shear wave velocities, Poisson's ratios and Moho depths. *Geophysical Journal International*, 211(3):1328–1340, 2017. doi: 10.1093/gji/ggx333.

Reading, A. M. and Heintz, M. Seismic anisotropy of East Antarctica from shear-wave splitting: Spatially varying contributions from lithospheric structural fabric and mantle flow? *Earth Planet. Sci. Lett.*, 268(3-4):433–443, 2008. doi: 10.1016/j.epsl.2008.01.041.

Ritzwoller, M. H., Shapiro, N. M., Levshin, A. L., and Leahy, G. M. Crustal and upper mantle structure beneath Antarctica and surrounding oceans. *J. Geophys. Res.: Solid Earth*, 106(B12):30645–30670, 2001. doi: 10.1029/2001JB000179.

Roult, G., Rouland, D., and Montagner, J. Antarctica II: Upper-mantle structure from velocities and anisotropy. *Phys. Earth Planet. Inter.*, 84 (1-4):33–57, 1994. doi: 10.1016/0031-9201(94)90033-7.

Salimbeni, S., Pondrelli, S., Danesi, S., and Morelli, A. Seismic anisotropy of the Victoria Land region, Antarctica. *Geophysical Journal International*, 182(1):421–432, 2010. doi: 10.1111/j.1365-246x.2010.04624.x.

Savage, M. K. Seismic anisotropy and mantle deformation: What have we learned from shear wave splitting? *Reviews of Geophysics*, 37(1): 65 – 106, 1999. doi: 10.1029/98rg02075.

Shen, W., Wiens, D. A., Anandakrishnan, S., Aster, R. C., Gerstoft, P., Bromirski, P. D., Hansen, S. E., Dalziel, I. W., Heeszel, D. S., Huerta, A. D., Nyblade, A. A., Stephen, R., Wilson, T. J., and Winberry, J. P. The crust and upper mantle structure of central and West Antarctica from Bayesian inversion of Rayleigh wave and receiver functions. *J. Geophys. Res.: Solid Earth*, 123(9):7824–7849, 2018. doi: 10.1029/2017JB015346.

Sieminski, A., Debayle, E., and Lévêque, J.-J. Seismic evidence for deep low-velocity anomalies in the transition zone beneath West Antarctica. *Earth Planet. Sci. Lett.*, 216(4):645–661, 2003. doi: 10.1016/S0012-821X(03)00518-1.

Silver, P. G. Seismic anisotropy beneath the continents: Probing the depths of geology. *Annu. Rev. Earth Planet. Sci.*, 24, 1996. doi: 10.1146/annurev.earth.24.1.385.

Silver, P. G. and Chan, W. W. Implications for continental structure and evolution from seismic anisotropy. *Nature*, 335(6185):34–39, 1988. doi: 10.1038/335034a0.

Smith, D. B., Ritzwoller, M. H., and Shapiro, N. M. Stratification of anisotropy in the Pacific upper mantle. *J. Geophys. Res.*, 109(B11):243 – 22, 2004. doi: 10.1029/2004jb003200.

Snyder, D. and Bruneton, M. Seismic anisotropy of the Slave craton, NW Canada, from joint interpretation of SKS and Rayleigh waves. *Geophysical Journal International*, 169(1):170–188, 04 2007. doi: 10.1111/j.1365-246X.2006.03287.x.

Stutzmann, E. and Montagner, J.-P. An inverse technique for retrieving higher mode phase velocity and mantle structure. *Geophys. J. Int.*, 113(3):669–683, 1993. doi: 10.1111/j.1365-246X.1993.tb04659.x.

Tozer, B., Sandwell, D. T., Smith, W. H., Olson, C., Beale, J., and Wessel, P. Global bathymetry and topography at 15 arc sec: SRTM15+. *Earth Space Sci.*, 6(10):1847–1864, 2019. doi: 10.1029/2019EA000658.

Trampert, J. and van Heijst, H. J. Global azimuthal anisotropy in the transition zone. *Science*, 296(5571):1297–1299, 2002. doi: 10.1126/science.1070264.

Trampert, J. and Woodhouse, J. H. Global anisotropic phase velocity maps for fundamental mode surface waves between 40 and 150 s. *Geophys. J. Int.*, 154(1):154–165, 2003. doi: 10.1046/j.1365-246X.2003.01952.x.

Visser, K. *Monte Carlo search techniques applied to the measurement of higher mode phase velocities and anisotropic surface wave tomography. Geologica Ultraiectina (285)*. Departement Aardwetenschappen, 2008. OCLC: 6893359236.

Visser, K., Lebedev, S., Trampert, J., and Kennett, B. Global Love wave overtone measurements. *Geophysical Research Letters*, 34(3), 2007.

Volk, O., White, R. S., Pilia, S., Green, R. G., Maclennan, J., and Rawlinson, N. Oceanic crustal flow in Iceland observed using seismic anisotropy. *Nature Geoscience*, 14(3):168–173, 2021. doi: 10.1038/s41561-021-00702-7.

Watson, T., Nyblade, A., Wiens, D. A., Anandakrishnan, S., Benoit, M., Shore, P. J., Voigt, D., and VanDecar, J. P and S velocity structure of the upper mantle beneath the Transantarctic Mountains, East Antarctic craton, and Ross Sea from travel time tomography. *Geochemistry, Geophysics, Geosystems*, 7(7), 2006. doi: 10.1029/2005gc001238.

Wiens, D. and Nyblade, A. A Broadband Seismic Experiment to Image the Lithosphere beneath the Gamburtsev Mountains, East Antarctica, 2007a.

Wiens, D. and Nyblade, A. IPY POLENET-Antarctica: Investigating links between geodynamics and ice sheets, 2007b.

Winberry, J. P. and Anandakrishnan, S. Crustal structure of the West Antarctic rift system and Marie Byrd Land hotspot. *Geology*, 32(11): 977–980, 2004. doi: 10.1130/g20768.1.

Wirth, E. A. and Long, M. D. A contrast in anisotropy across mid-lithospheric discontinuities beneath the central United States—A relic of craton formation. *Geology*, 42(10):851–854, 2014. doi: 10.1130/g35804.1.

Woodhouse, J. The coupling and attenuation of nearly resonant multiplets in the Earth's free oscillation spectrum. *Geophysical Journal of the Royal Astronomical Society*, 61(2):261 – 283, 1980. doi: 10.1111/j.1365-246x.1980.tb04317.x.

Wörner, G. Lithospheric dynamics and mantle sources of alkaline magmatism of the Cenozoic West Antarctic Rift System. *Global and Planetary Change*, 23(1-4):61–77, 1999. doi: 10.1016/S0921-8181(99)00051-X.

Xu, H. and Beghein, C. Measuring higher mode surface wave dispersion using a transdimensional Bayesian approach. *Geophys. J. Int.*, 218 (1):333–353, 2019. doi: 10.1093/gji/ggz133.

Yoshizawa, K. and Ekström, G. Automated multimode phase speed measurements for high-resolution regional-scale tomography: application to North America. *Geophysical Journal International*, 183(3):1538–1558, 2010.

Yoshizawa, K. and Kennett, B. Non-linear waveform inversion for surface waves with a neighbourhood algorithm—application to multimode dispersion measurements. *Geophysical Journal International*, 149(1):118–133, 2002.

Yoshizawa, K. and Kennett, B. Multimode surface wave tomography for the Australian region using a three-stage approach incorporating finite frequency effects. *J. Geophys. Res.: Solid Earth*, 109(B2), 2004. doi: 10.1029/2002JB002254.

Yuan, H. and Romanowicz, B. Lithospheric layering in the North American craton. *Nature*, 466(7310):1063–1068, 2010.

Yuan, H., Romanowicz, B., Fischer, K. M., and Abt, D. L. 3-D shear wave radially and azimuthally anisotropic velocity model of the North American upper mantle. *Geophysical Journal of the Royal Astronomical Society*, 184(3):1237 – 1260, 2011. doi: 10.1111/j.1365-246x.2010.04901.x.

Yuan, K. and Beghein, C. Seismic anisotropy changes across upper mantle phase transitions. *Earth Planet. Sci. Lett.*, 374:132–144, 2013.

Yuan, K. and Beghein, C. Three-dimensional variations in Love and Rayleigh wave azimuthal anisotropy for the upper 800 km of the mantle.

J. Geophys. Res.: Solid Earth, 119(4):3232–3255, 2014.

Zhang, H., Zhao, D., Ju, C., Li, Y. E., Li, G., Ding, M., Chen, S., and Zhao, J. Upper Mantle Deformation of the Terror Rift and Northern Transantarctic Mountains in Antarctica: Insight From P Wave Anisotropic Tomography. *Geophys. Res. Lett.*, 47(9), 2020. doi: 10.1029/2019gl086511.

Zhou, Z., Wiens, D. A., Shen, W., Aster, R. C., Nyblade, A., and Wilson, T. J. Radial Anisotropy and Sediment Thickness of West and Central Antarctica Estimated From Rayleigh and Love Wave Velocities. *Journal of Geophysical Research: Solid Earth*, 127(3), 2022. doi: 10.1029/2021jb022857.

Zhou, Z., Wiens, D. A., Nyblade, A., Aster, R. C., Wilson, T. J., and Shen, W. Crustal and Uppermost Mantle Azimuthal Seismic Anisotropy of Antarctica from Ambient Noise Tomography. *Journal of Geophysical Research: Solid Earth*, 2023. submitted.

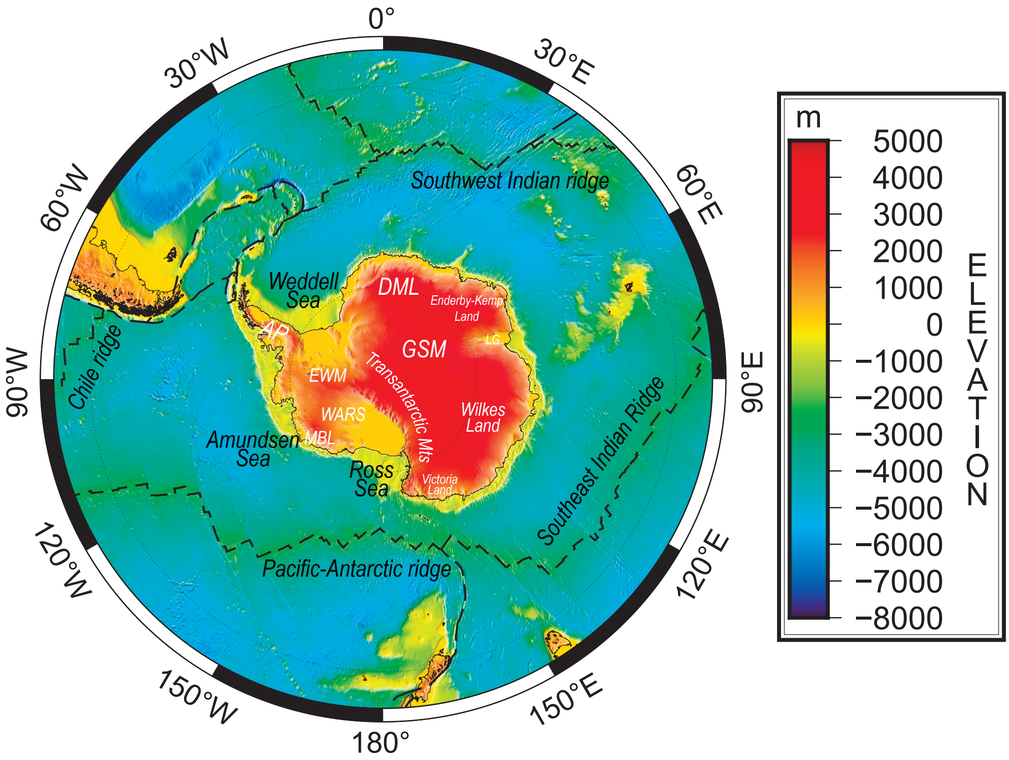

Figure 1 Topographic and bathymetric map of Antarctica and surrounding areas based on model SRTM15+ (Tozer et al., 2019). AP = Antarctica Peninsula; DML = Dronning Maud Land; EWM = Ellsworth-Whitmore Mountains; GSM = Gamburtsev Subglacial Mountains; LG = Lambert Graben; WARS = West Antarctic rift system. Ocean ridges are indicated by the dashed lines.

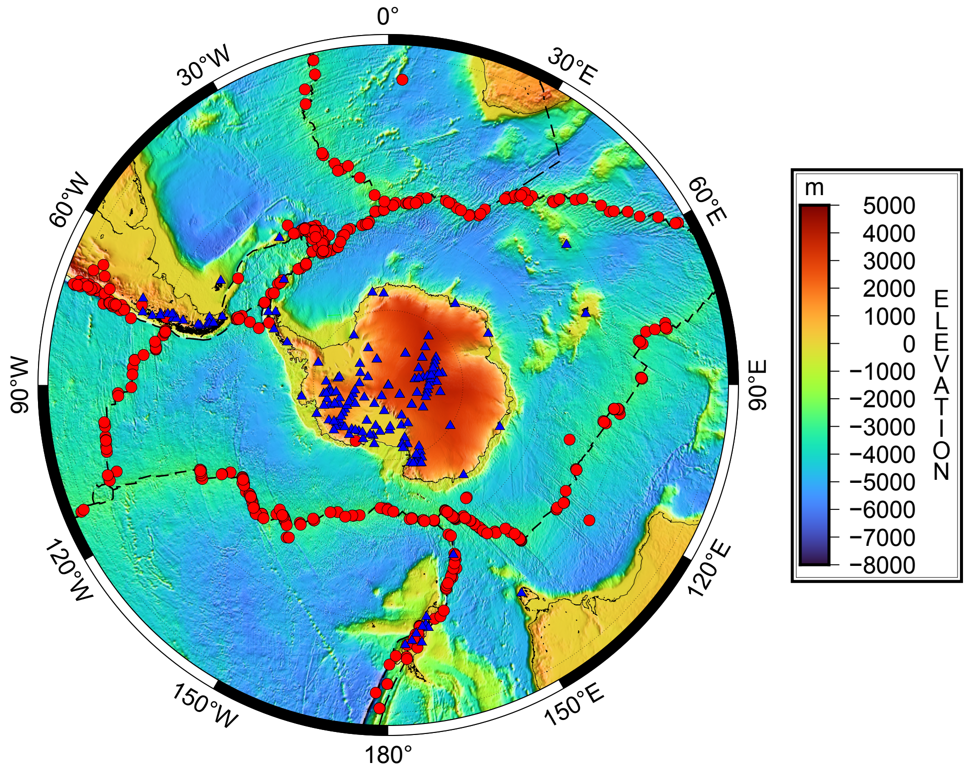

Figure 2 Maps of the selected event location (red circles) and stations (blue triangles) superimposed to bathymetry and topography (Tozer et al., 2019). Ocean ridges are shown by the dashed black lines.

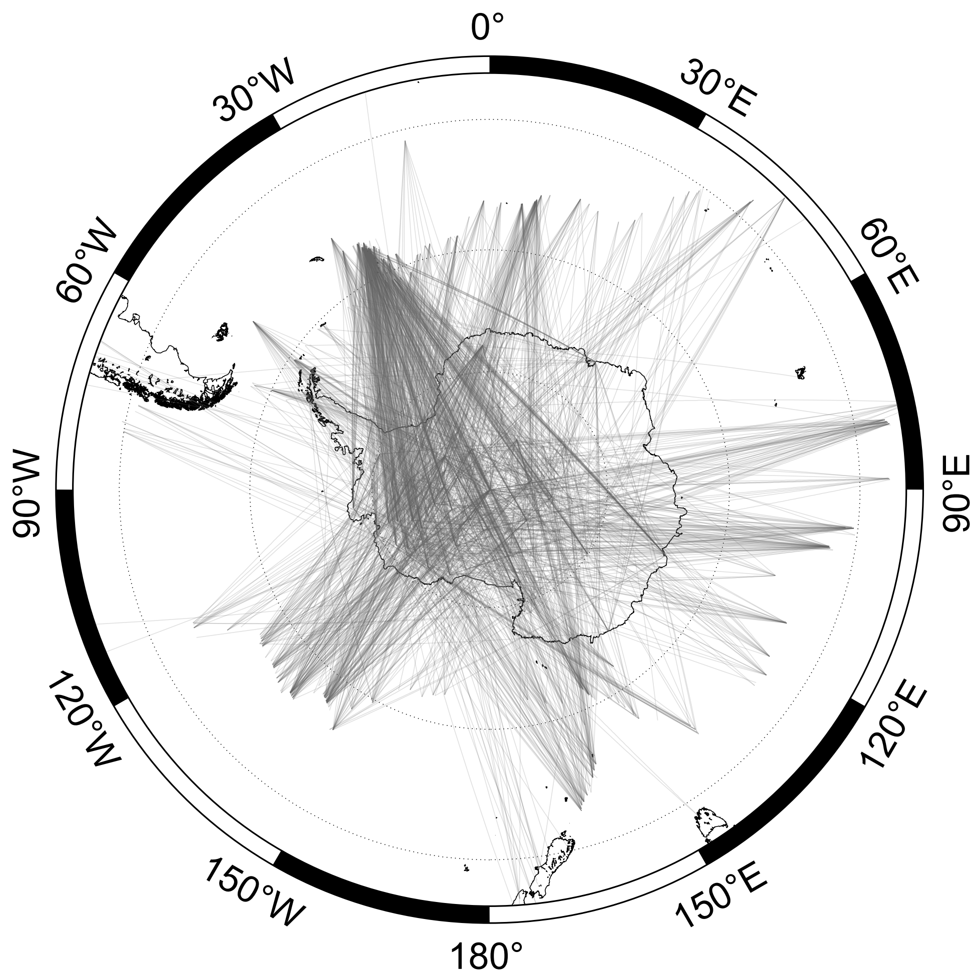

Figure 3 Ray-path coverage of all event-station pairs which passed all quality control steps.

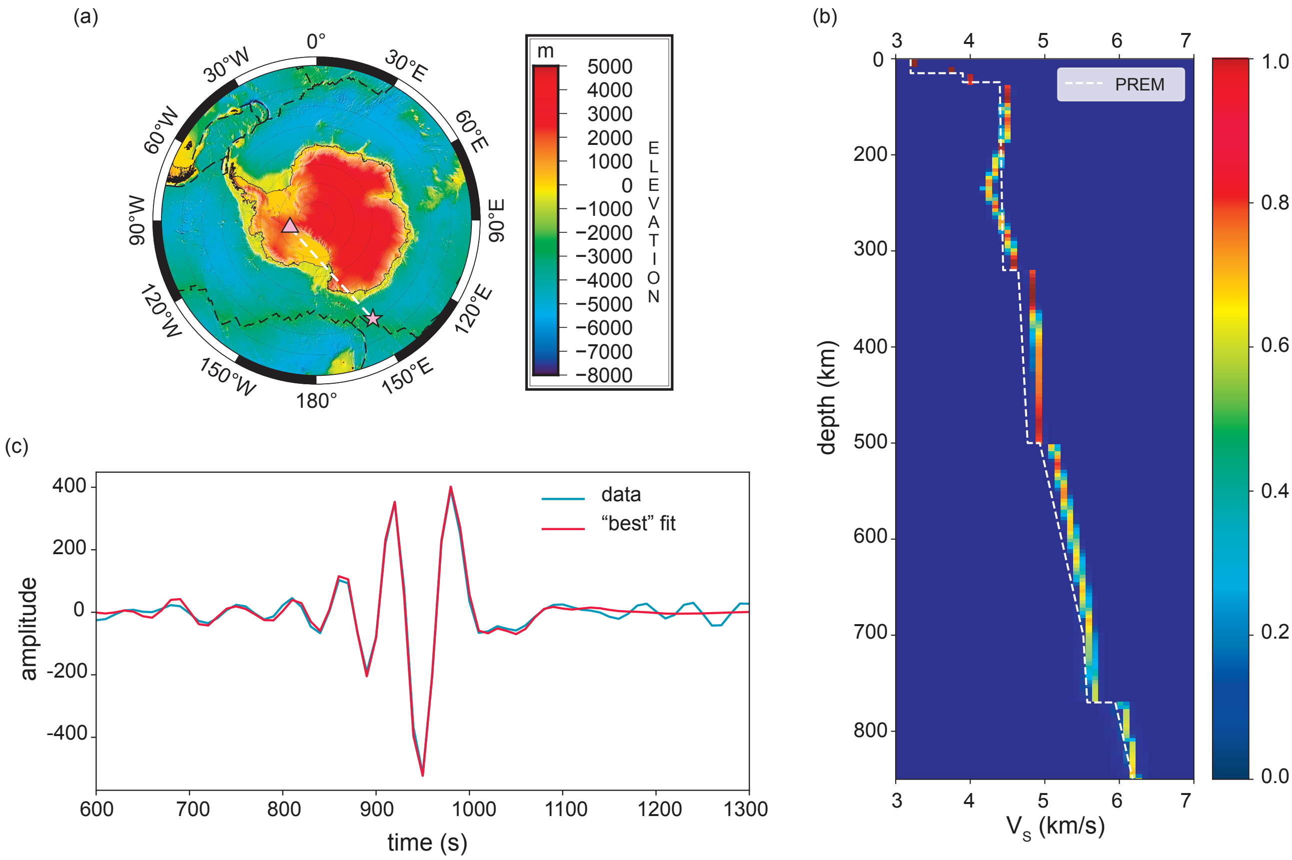

Figure 4 Illustration of the MCMC method employed. (a) Topographic map of Antarctica with selected station (triangle) and event (star). Plate boundaries are shown by the dashed black lines. (b) The resulting distribution of velocity models between the selected event-station pair. The color scale represents the likelihood of the model at a given depth. PREM is shown for reference. (c) Waveform fit for one of the best-fitting models.

Table 1 Selection of frequency-time windows. The first and second window indices correspond to the fundamental mode and the third window is for higher modes. The first and third windows share the same start time, which is determined by the S- or SS-wave arrival times. All other start/end times are determined by Δ/U, where Δ is the event epicentral distance and the values of the group velocities U are indicated in the table.

Window index	Frequency(mHz)	Start	End
1	5-10	S or SS	$U = 2.95\ km/s$
2	10-20	$U = 4.30\ km/s$	$U = 3.20\ km/s$
3	10-20	S or SS	$U = 4.30\ km/s$

Table 2 Significance of 2Ψ and 4Ψ terms at different depths from F-test analysis. A lower probability means that the model with more parameters has significantly lower misfits compared to the model with fewer parameters, and thus those extra parameters are needed to explain the data.

Depth	P(iso + 2Ψ == iso)	P(iso + 2Ψ + 4Ψ == iso + 2Ψ)
60 km	0.23%	6.62%
150 km	4.40%	37.50%
200 km	2.98%	35.41%
250 km	12.56%	39.50%
350 km	15.19%	30.09%
450 km	19.67%	44.74%
600 km	34.21%	25.54%

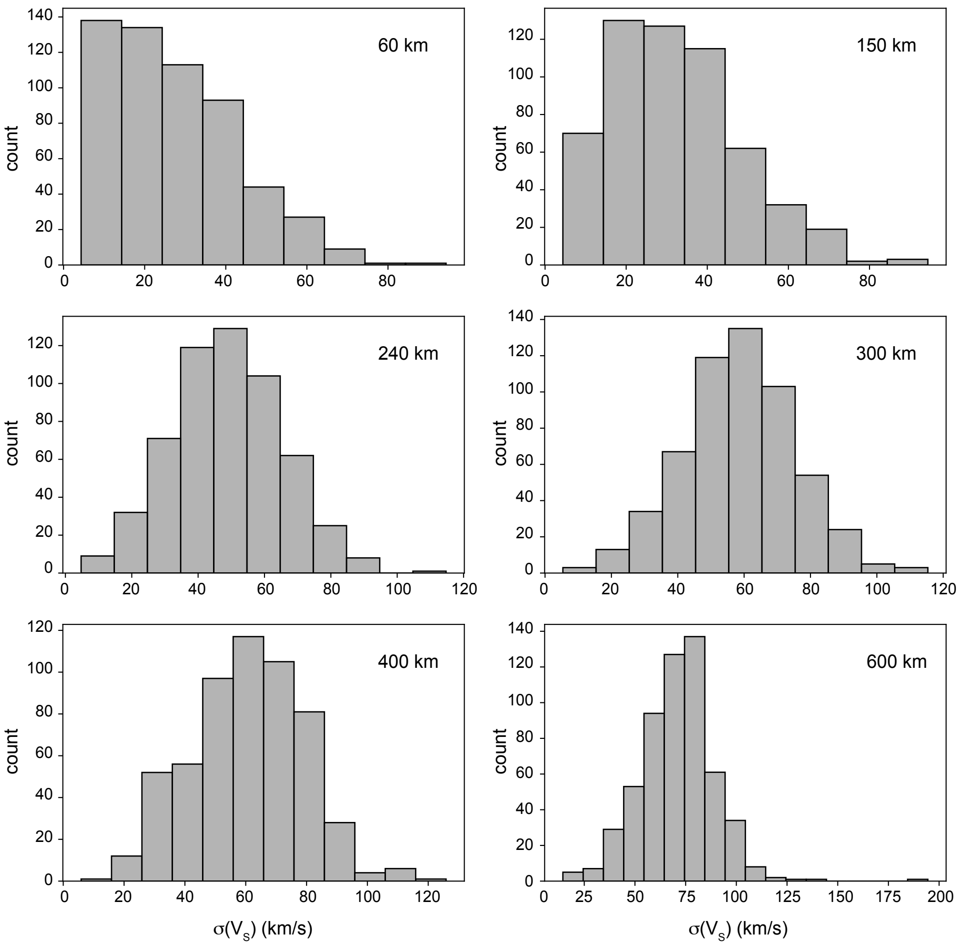

Figure 5 Distribution of path-averaged velocity $V_{SV}(z)$ standard deviations at different depths. All paths shown in Fig. 3 were included, and the standard deviation for each path is calculated from the ensemble of models obtained by our MCMC algorithm.

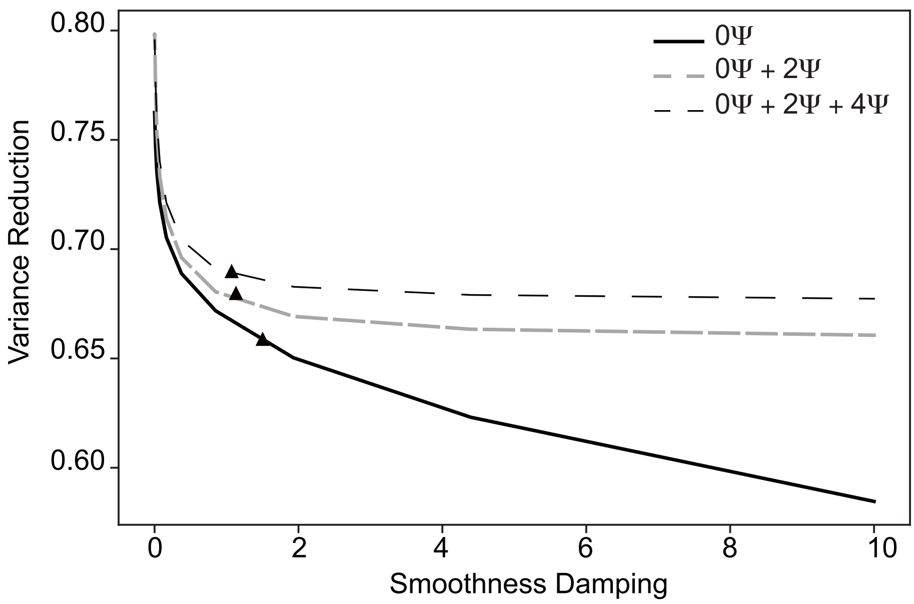

Figure 6 Example of damping parameter selection based on the L-curve method. The optimal damping parameters are selected at the elbow of the curves and are denoted by triangles. We first searched for the damping parameters for the 0Ψ-term. The $0\Psi + 2\Psi$ curve was obtained by fixing the selected isotropic damping parameter and changing the 2Ψ-term damping. The $0\Psi + 2\Psi + 4\Psi$ curve resulted from varying the 4Ψ damping parameter while fixing the isotropic and 2Ψ-term damping parameters.

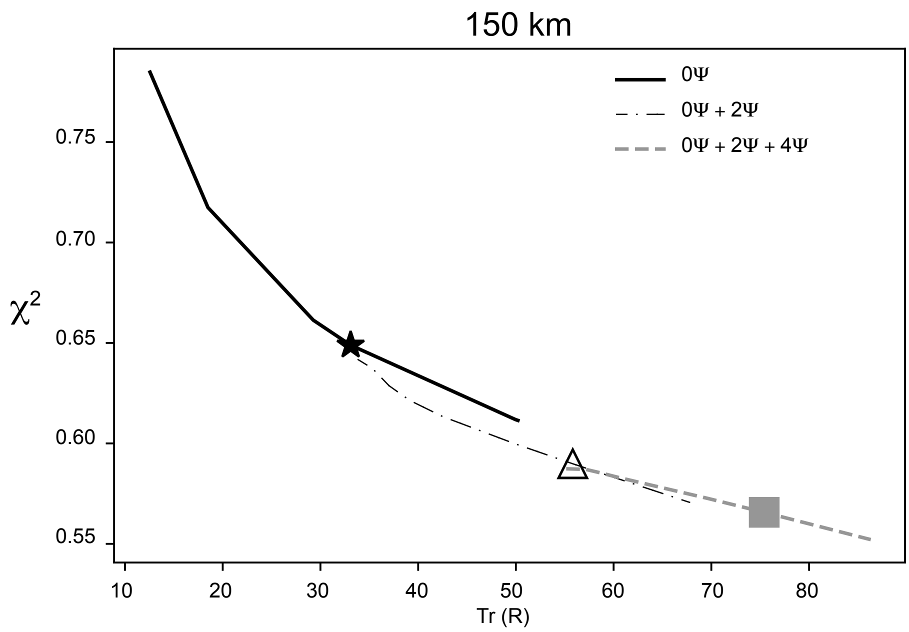

Figure 7 Example of reduced χ^2 as a function of the trace of the resolution matrix $\mathbf{R}$ for inversions at 150 km depth. The solid black curve is for inversions of the isotropic terms only. Different values of the trace of the resolution matrix were obtained by applying different levels of damping. The preferred model selected by the L-curve method is marked by the black star. The thin black curve represents the inversion with both isotropic and 2Ψ terms with fixed isotropic damping parameter (corresponding to the value at the black star). The grey dashed curve is based on the selected 0Ψ and 2Ψ damping parameters for different values of the 4Ψ parameter. The triangle and the square correspond to the models selected with the L-curve method for the $0\Psi + 2\Psi$ and $0\Psi + 2\Psi + 4\Psi$ inversions, respectively.

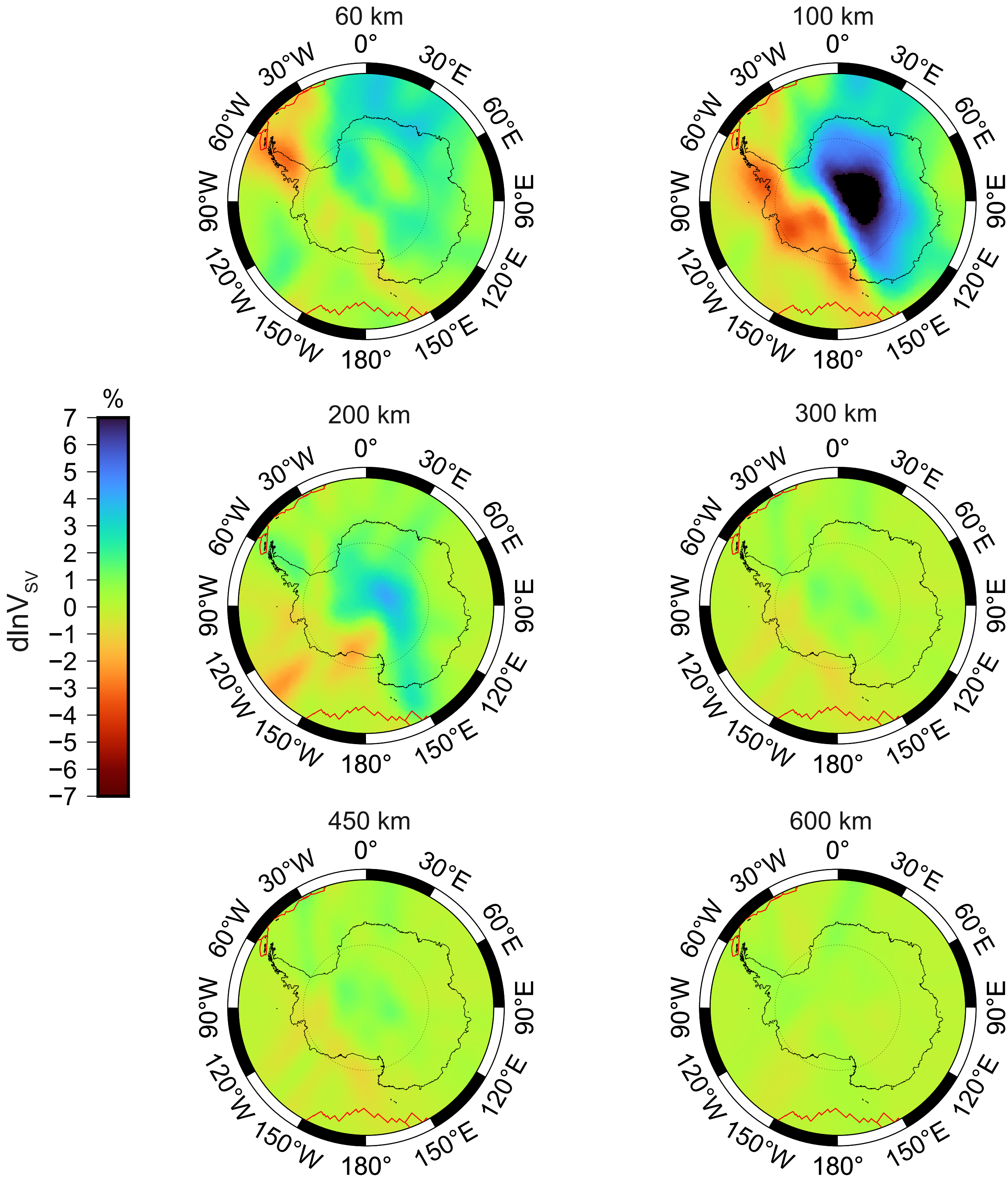

Figure 8 Isotropic part of our 3-D model at different depths. Perturbations are given with respect to PREM (Dziewonski and Anderson, 1981).

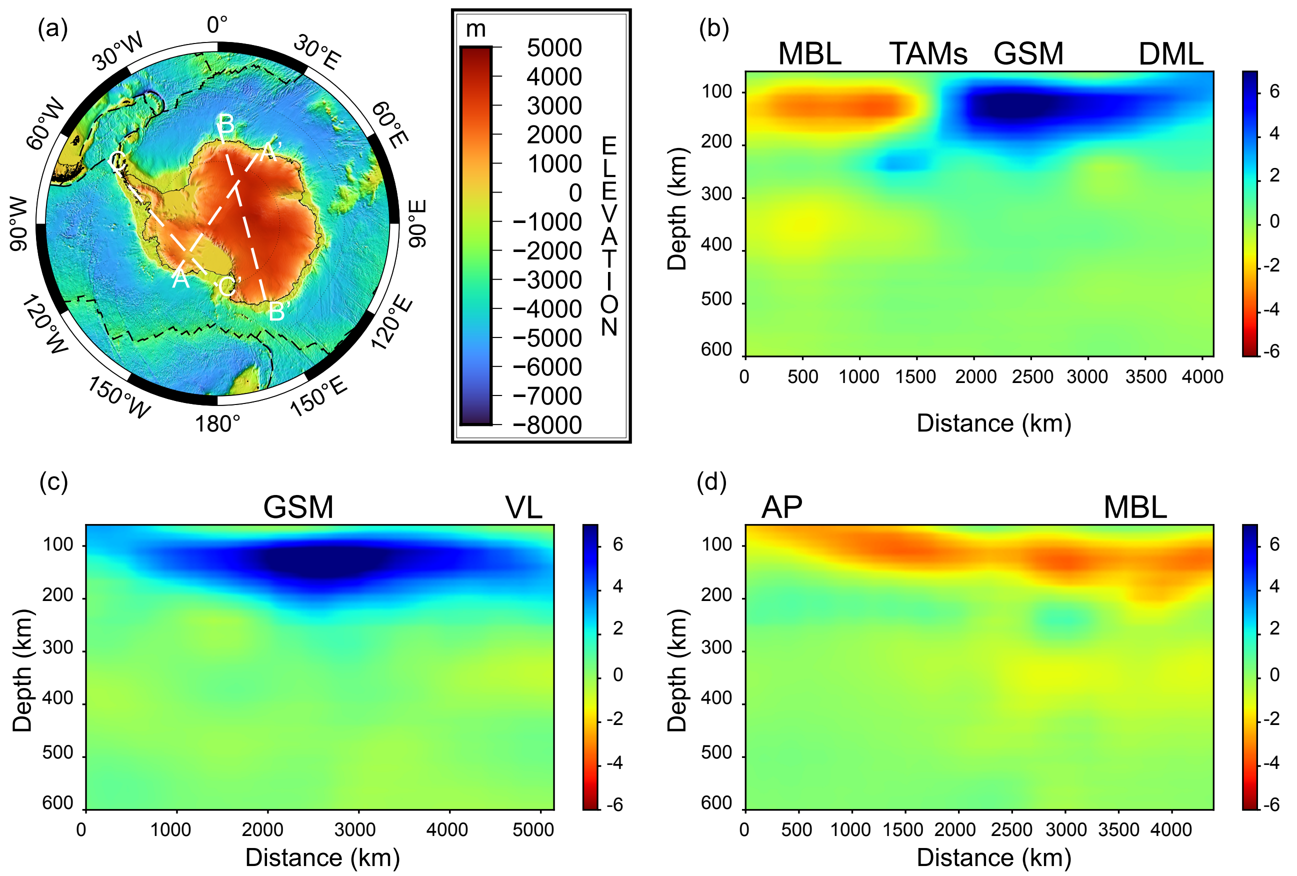

Figure 9 Cross sections of our 3-D isotropic model. V_S is shown along the transects shown by dashed lines in the topographic map of Antarctica (a): A-A'(b), which crosses EANT and WANT, B-B'(c), which samples EANT, and C-C'(c), which crosses WANT. Abbreviations: AP = Antarctica Peninsula; DML = Dronning Maud Land; GSM = Gamburtsev Subglacial Mountains; TAMs = Transantarctic Mountains; VL = Victoria Land.

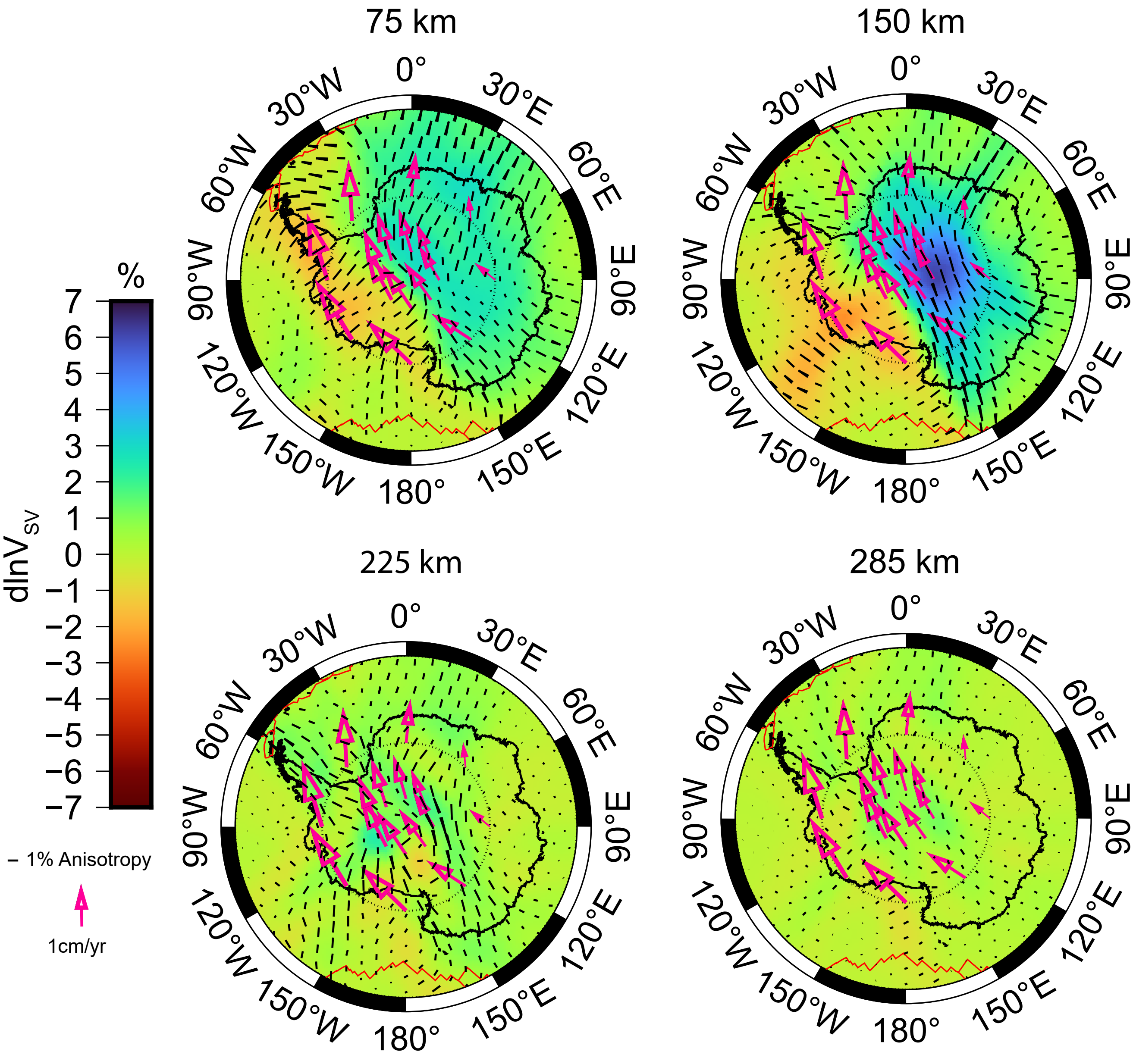

Figure 10 2Ψ anisotropy model at different depths superimposed onto the isotropic part of the model. The black bars represent the fast direction for V_{SV} propagation and the length of the black bars is proportional to the strength of the anisotropy. The magenta arrows represent the APM direction based on NUVEL-1A with no-net rotation reference frames (Gripp and Gordon, 2002).

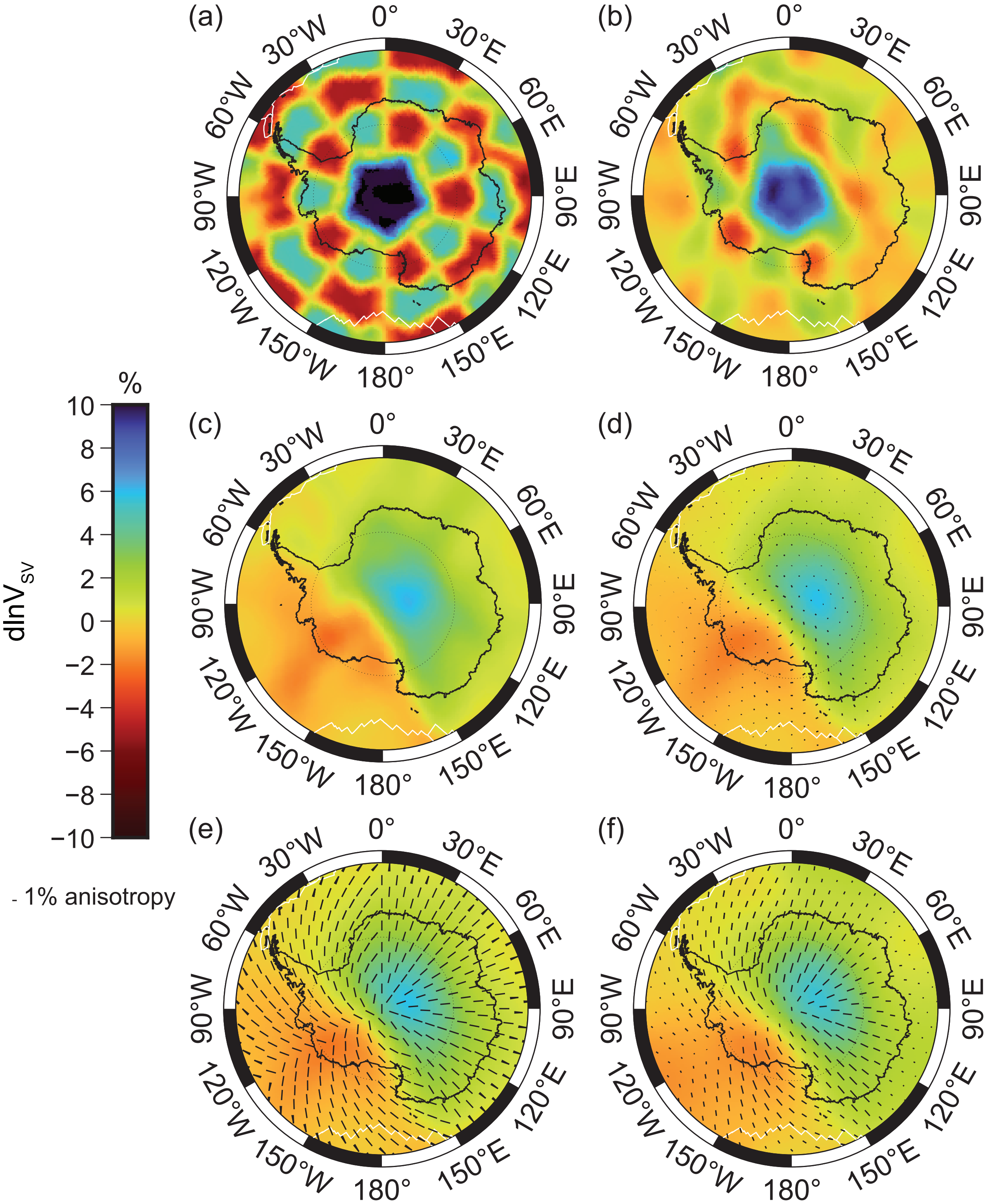

Figure 11 Synthetic tests at 150 km depth with the input models on the left and the corresponding output models on the right. (top): Isotropic checkerboard test; (middle): 2Ψ anisotropic inversion of an isotropic input model; (bottom): 2Ψ anisotropic resolution test. The length of the black bars represents the amplitudes of the anisotropy.

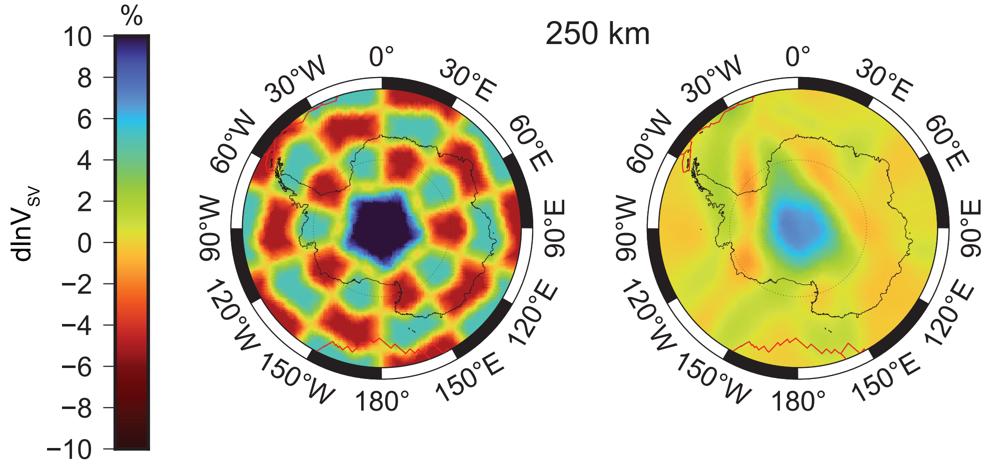

Figure 12 Synthetic tests at 250 km depth with isotropic checkerboard input model on the left and the corresponding output models on the right.

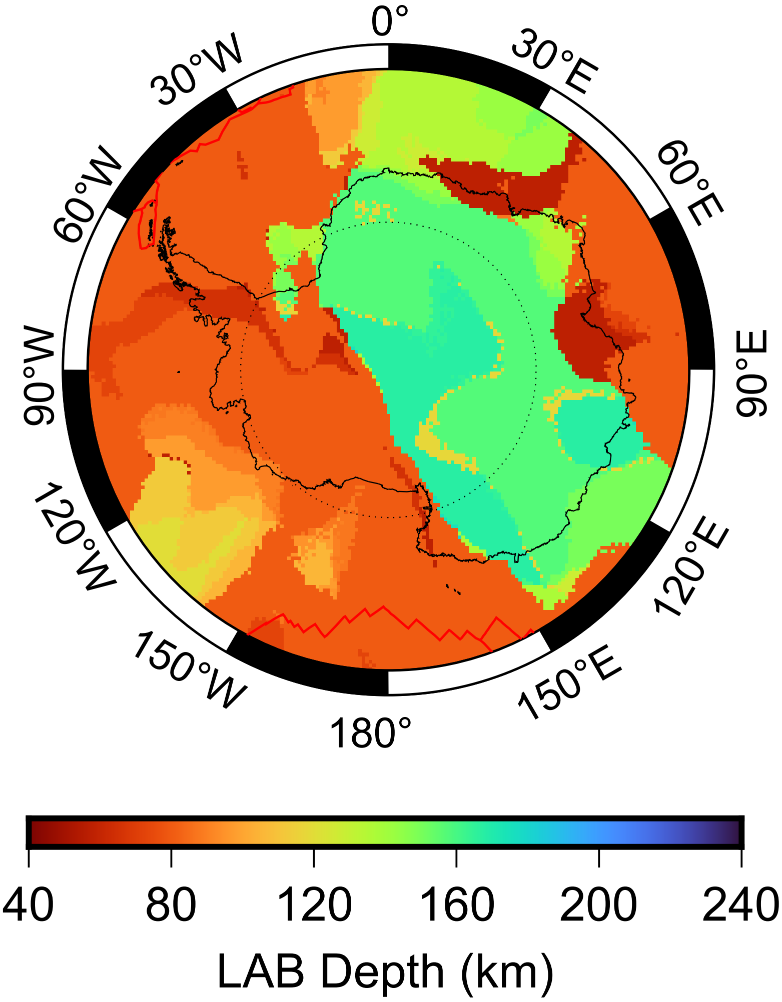

Figure 13 Map of the estimated LAB depth based on the middle of the interval over which V_{SV} decreases in the isotropic part of the model.

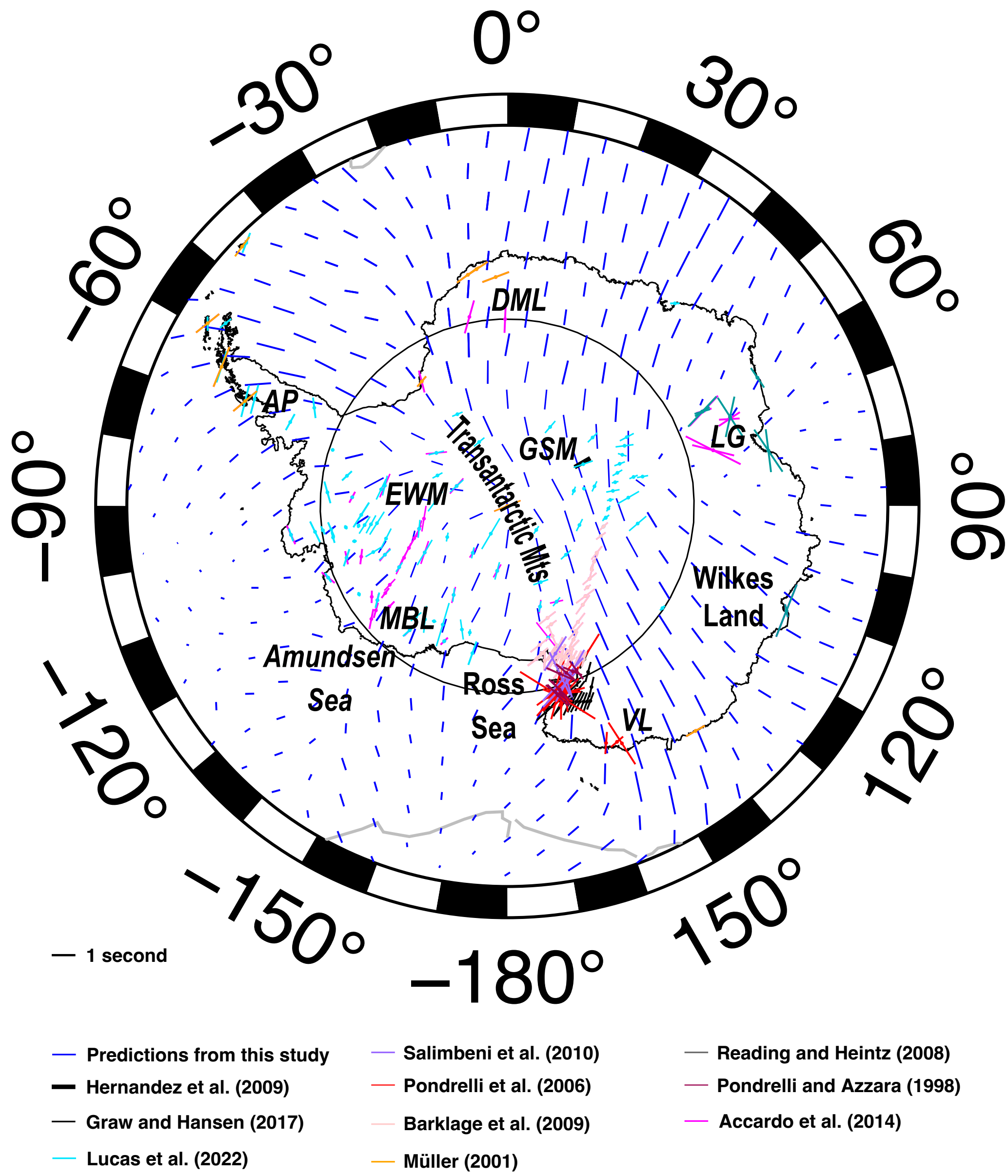

Figure 14 Predicted (blue) and observed shear-wave splitting for Antarctica. The thick black bar represents the overall splitting directions and study area from Hernandez et al. (2009). Others studies are from Pondrelli and Azzara (1998), Müller (2001), Pondrelli et al. (2006), Reading and Heintz (2008), Barklage et al. (2009), Accardo et al. (2014), Graw and Hansen (2017), and Lucas et al. (2022). The length of the bars is proportional to the splitting delay times. The plate boundaries are shown in grey. DML = Dronning Maud Land; EWM = Ellsworth-Whitmore Mountains; GSM = Gamburtsev Subglacial Mountains; LG = Lambert Graben; MBL = Marie Byrd Land; AP = Antarctica Peninsula; VL = Victoria Land.